Published for SISSA by Springer

Received: December 12, 2014
Revised: January 15, 2015
Accepted: January 18, 2015
Published: February 11, 2015

Heavy Majorana neutrinos from $W\gamma$ fusion at hadron colliders

Daniel Alva,[a,b] **Tao Han**[b,c] **and Richard Ruiz**[b]

[a] *Centro de Ciências Naturais e Humanas, Universidade Federal do ABC, Santo André, SP 09210-170, Brazil*
[b] *Pittsburgh Particle physics, Astronomy, and Cosmology Center Department of Physics & Astronomy, University of Pittsburgh, Pittsburgh, PA 15260, U.S.A.*
[c] *Korea Institute for Advanced Study (KIAS), Seoul 130-012, Korea*

E-mail: danalva@pitt.edu, than@pitt.edu, rer50@pitt.edu

Abstract: Vector boson fusion processes become increasingly more important at higher collider energies and for probing larger mass scales due to collinear logarithmic enhancements of the cross section. In this context, we revisit the production of a hypothetic heavy Majorana neutrino (N) at hadron colliders. Particular attention is paid to the fusion process $W\gamma \to N\ell^{\pm}$. We systematically categorize the contributions from a photon initial state in the elastic, inelastic, and deeply inelastic channels. Comparing with the leading channel via the Drell-Yan production $q\bar{q}' \to W^* \to N\ell^{\pm}$ at NNLO in QCD, we find that the $W\gamma$ fusion process becomes relatively more important at higher scales, surpassing the DY mechanism at $m_N \sim 1$ TeV (770 GeV), at the 14 TeV LHC (100 TeV VLHC). We investigate the inclusive heavy Majorana neutrino signal, including QCD corrections, and quantify the Standard Model backgrounds at future hadron colliders. We conclude that, with the currently allowed mixing $|V_{\mu N}|^2 < 6 \times 10^{-3}$, a 5σ discovery can be made via the same-sign dimuon channel for $m_N = 530$ (1070) GeV at the 14 TeV LHC (100 TeV VLHC) after 1 ab^{-1}. Reversely, for $m_N = 500$ GeV and the same integrated luminosity, a mixing $|V_{\mu N}|^2$ of the order 1.1×10^{-3} (2.5×10^{-4}) may be probed.

Keywords: Beyond Standard Model, Neutrino Physics

ArXiv ePrint: 1411.7305

doi:10.1007/JHEP02(2015)072

JHEP02(2015)072

Contents

1 Introduction

The discovery of the Higgs boson completes the Standard Model (SM). Yet, the existence of nonzero neutrino masses remains one of the clearest indications of physics beyond the Standard Model (BSM) [1–8] The simplest SM extension that can simultaneously explain both the existence of neutrino masses and their smallness, the so-called Type I seesaw mechanism [9–18], introduces a right handed (RH) neutrino N_R. Via a Yukawa coupling

JHEP02(2015)072

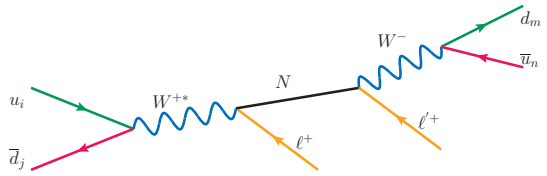

(a)

Figure 1. Diagram representing resonant heavy Majorana neutrino production through the DY process and its decay into same-sign leptons and dijet. All diagrams drawn using JaxoDraw [38].

y_ν, the resulting Dirac mass is $m_D = y_\nu \langle \Phi \rangle$, where Φ is the SM Higgs SU(2)$_L$ doublet. As N_R is a SM-gauge singlet, one could assign N_R a Majorana mass m_M without violating any fundamental symmetry of the model. Requiring that $m_M \gg m_D$, the neutrino mass eigenvalues are

$$m_1 \sim m_D \frac{m_D}{m_M} \quad \text{and} \quad m_2 \sim m_M. \tag{1.1}$$

Thus, the apparent smallness of neutrino masses compared to other fermion masses is due to the suppression by a new scale above the EW scale. Taking the Yukawa coupling to be $y_\nu \sim \mathcal{O}(1)$, the Majorana mass scale must be of the order 10^{13} GeV to recover sub-eV light neutrinos masses. However, if the Yukawa couplings are as small as the electron Yukawa coupling, i.e., $y_\nu \lesssim \mathcal{O}(10^{-5})$, then the mass scale could be at $\mathcal{O}(1)$ TeV or lower [19–22].

Given the lack of guidance from theory of lepton flavor physics, searches for Majorana neutrinos must be carried out as general and model-independent as possible. Low-energy phenomenology of Majorana neutrinos has been studied in detail [21–37]. Studied first in ref. [23] and later in refs. [24–29], the production channel most sensitive to heavy Majorana neutrinos (N) at hadron colliders is the resonant Drell-Yan (DY) process,

$$pp \to W^{\pm *} \to N\ \ell^\pm, \quad \text{with} \quad N \to W^\mp\ \ell'^\pm, \quad W^\mp \to j\ j, \tag{1.2}$$

in which the same-sign dilepton channel violates lepton number L by two units ($\Delta L = 2$); see figure 1. Searches for eq. (1.2) are underway at LHC experiments [39–41]. Non-observation in the dimuon channel has set a lower bound on the heavy neutrino mass of 100 (300) GeV for mixing $|V_{\mu N}|^2 = 10^{-2\ (-1)}$ [40]. Bounds on mixing from $0\nu\beta\beta$ [42, 43] and EW precision data [44–47] indicate that the 14 TeV LHC is sensitive to Majorana neutrinos with mass between 10 and 375 GeV after 100 fb^{-1} of data [27]. Recently renewed interest in a very large hadron collider (VLHC) with a center of mass (c.m.) energy about 100 TeV, which will undoubtedly extend the coverage, suggests a reexamination of the search strategy at the new energy frontier.

Production channels for heavy Majorana neutrinos at higher orders of α were systematically cataloged in ref. [26]. Recently, the vector boson fusion (VBF) channel $W\gamma \to N\ell^\pm$ was studied at the LHC, and its t-channel enhancement to the total cross section was emphasized [36]. Along with that, they also considered corrections to the DY process by including the tree-level QCD contributions to $N\ell^\pm$+jets. Significant enhancement was claimed over both the leading order (LO) DY signal [27, 29] and the expected next-to-

JHEP02(2015)072

Figure 2. Diagrammatic representation of (a) elastic and (b) inelastic/deeply inelastic γp scattering.

next-to-leading order (NNLO) in QCD-corrected DY rate [48], prompting us to revisit the issue.

We carry out a systematic treatment of the photon-initiated processes. The elastic emission (or photon emission off a nucleon) at colliders, as shown in figure 2(a), is of considerable interest for both SM [49–55] and BSM processes [56–59, 61–65], and has been observed at electron [66], hadron [67, 68], and lepton-hadron [69, 70] colliders. The inelastic (collinear photon off a quark) and deeply inelastic (large momentum transfer off a quark) channels, as depicted in figure 2(b), may take over at higher momentum transfers [52, 71, 72]. Comparing with the DY production $qq' \to W^* \to N\ell^\pm$, we find that the $W\gamma$ fusion process becomes relatively more important at higher scales, taking over the QCD-corrected DY mechanism at $\gtrsim 1$ TeV (770 GeV) at the 14-TeV LHC (100 TeV VLHC). At $m_N \sim 375$ GeV, a benchmark value presented in [29], we find the $W\gamma$ contribution to be about 20% (30%) of the LO DY cross section.

NNLO in QCD corrections to the DY processes are well-known [48] and the K-factor for the inclusive cross sections are about $1.2-1.4$ $(1.2-1.5)$ at LHC (VLHC) energies. Taking into account all the contributions, we present the state-of-the-art results for the inclusive production of heavy neutrinos in 14 and 100 TeV pp collisions. We further perform a signal-versus-background analysis for a 100 TeV collider of the fully reconstructible and L-violating final state in eq. (1.2). With the currently allowed mixing $|V_{\mu N}|^2 < 6 \times 10^{-3}$, we find that the 5σ discovery potential of ref. [29] can be extended to $m_N = 530$ (1070) GeV at the 14 TeV LHC (100 TeV VLHC) after 1 ab^{-1}. Reversely, for $m_N = 500$ GeV and the same integrated luminosity, a mixing $|V_{\mu N}|^2$ of the order 1.1×10^{-3} (2.5×10^{-4}) may be probed. Our results are less optimistic than reported in [36]. We attribute the discrepancy to their significant overestimate of the signal in the tree-level QCD calculations, as quantified in section 2.3.4.

The rest of paper is organized as follows: in section 2, we describe our treatment of the several production channels considered in this study, address the relevant scale dependence, and present the inclusive $N\ell^\pm$ rate at the 14 TeV LHC and 100 TeV VLHC. In section 3, we perform the signal-versus-background analysis at a future 100 TeV pp collider and report the discovery potential. Finally summarize and conclude in section 4. Appendices A and B present the details of the photon PDF's for the elastic and inelastic channels, respectively. Appendix C gives our treatment for the Poisson statistics.

JHEP02(2015)072

2 Heavy N production at hadron colliders

For the production of a heavy Majorana neutrino at hadron colliders, the leading channel is the DY process at order α^2 (LO) [23]

$$q\,\overline{q}' \to W^{\pm *} \to N\,\ell^{\pm}. \tag{2.1}$$

The QCD corrections to DY-type processes up to α_s^2 (NNLO) are known [48], and will be included in our later analyses. Among other potential contributions, the next promising channel perhaps is the VBF channel [26]

$$W\,\gamma \to N\,\ell^{\pm}, \tag{2.2}$$

due to the collinear logarithmic enhancement from t-channel vector boson radiation. Formally of order α^2, there is an additional α suppression from the photon coupling to the radiation source. Collinear radiation off charged fermions (protons or quarks) leads to significant enhancement but requires proper treatment. In our full analysis, Ws are not considered initial-state partons [26] and all gauge invariant diagrams, including non-VBF contributions, are included.

We write the production cross section of a heavy state X in hadronic collisions as

$$\begin{aligned}
&\sigma(pp \to X + \text{anything}) \\
&\quad = \sum_{i,j} \int_{\tau_0}^1 d\xi_a \int_{\frac{\tau_0}{\xi_a}}^1 d\xi_b \left[f_{i/p}(\xi_a, Q_f^2) f_{j/p}(\xi_b, Q_f^2) \hat{\sigma}(ij \to X) + (i \leftrightarrow j) \right] \qquad (2.3) \\
&\quad = \int_{\tau_0}^1 d\tau \sum_{ij} \frac{d\mathcal{L}_{ij}}{d\tau}\, \hat{\sigma}(ij \to X). \qquad (2.4)
\end{aligned}$$

where $\xi_{a,b}$ are the fractions of momenta carried by initial partons (i, j), Q_f is the parton factorization scale, and $\tau = \hat{s}/s$ with $\sqrt{s}$ ($\sqrt{\hat{s}}$) the proton beam (parton) c.m. energy. For heavy neutrino production, the threshold is $\tau_0 = m_N^2/s$. Parton luminosities are given in terms of the parton distribution functions (PDFs) $f_{i,j/p}$ by the expression

$$\Phi_{ij}(\tau) \equiv \frac{d\mathcal{L}_{ij}}{d\tau} = \frac{1}{1+\delta_{ij}} \int_\tau^1 \frac{d\xi}{\xi} \left[f_{i/p}(\xi, Q_f^2) f_{j/p}\left(\frac{\tau}{\xi}, Q_f^2\right) + (i \leftrightarrow j) \right]. \tag{2.5}$$

We include the light quarks (u, d, c, s) and adopt the 2010 update of the CTEQ6L PDFs [73]. Unless stated otherwise, all quark (and gluon) factorization scales are set to half the c.m. energy:

$$Q_f = \sqrt{\hat{s}}/2. \tag{2.6}$$

For the processes with initial state photons (γ), their treatment and associated scale choices are given in section 2.3.

Our formalism and notation follow ref. [29]. For the heavy neutrino production via the SM charged current coupling, the cross section is proportional to the mixing parameter

JHEP02(2015)072

(squared) between the mass eigenstate N and the charged lepton ℓ (e, μ, τ). Thus it is convenient to factorize out the model-dependent parameter $|V_{\ell N}|^2$

$$\sigma(pp \to N\ell^{\pm}) \equiv \sigma_0(pp \to N\ell^{\pm}) \ \times \ |V_{\ell N}|^2, \tag{2.7}$$

where σ_0 will be called the "bare cross section". The branching fraction of a heavy neutrino to a particular lepton flavor ℓ is proportional to $|V_{N\ell}|^2 / \sum_{\ell'} |V_{N\ell'}|^2$. Thus for neutrino production and decay into same-sign leptons with dijet, it is similarly convenient to factorize out this ratio [27]:

$$\sigma(pp \to \ell^{\pm}\ell'^{\pm} + 2j) \equiv \sigma_0(pp \to \ell^{\pm}\ell'^{\pm} + 2j) \ \times \ S_{\ell\ell'}, \tag{2.8}$$

$$S_{\ell\ell'} \ = \ \frac{|V_{\ell N}|^2 |V_{\ell' N}|^2}{\sum_{\ell''} |V_{\ell'' N}|^2}. \tag{2.9}$$

The utility of this approach is that all the flavor-model dependence is encapsulated into a single, measurable number. Factorization into a bare rate and mixing coefficient holds generally for QCD and EW corrections as well.

2.1 Constraints on heavy neutrino mixing

As seen above in eq. (2.7), one of the most important model-dependent parameters to control the signal production rate is the neutrino mixing $V_{\ell N}$. Addressing the origin of lepton flavor is beyond the scope of this study, so masses and mixing factors are taken as independent, phenomenological parameters. We consider only the lightest, heavy neutrino mass eigenstate and require it to be kinematically accessible. Updates on heavy neutrino constraints can be found elsewhere [29, 34, 74]. Here we list only the most stringent bounds relevant to our analysis.

- **Bounds from $0\nu\beta\beta$**: for heavy Majorana neutrinos with $M_i \gg 1$ GeV, the absence of $0\nu\beta\beta$ decay restricts the mixing between heavy mass and electron-flavor eigenstates [42, 43]:

$$\sum_{m'} \frac{|V_{em'}|^2}{M_{m'}} < 5 \times 10^{-5} \text{ TeV}^{-1}. \tag{2.10}$$

- **Bounds from EW precision data**: mixing between a SM singlet above a few hundred GeV in mass and lepton flavor eigenstates is constrained by EW data [46]:

$$|V_{\mu N}|^2 < 3.2 \times 10^{-3}, \quad |V_{\tau N}|^2 < 6.2 \times 10^{-3} \quad \text{at} \quad 90\% \text{ C.L.} \tag{2.11}$$

We consider the existence of only the lightest heavy Majorana neutrino, which is equivalent to the decoupling limit where heavier eigenstates are taken to have infinite mass. Thus, for representative neutrino masses

$$m_N = 300 \ (500) \ [1000] \text{ GeV}, \tag{2.12}$$

we use the following mixing coefficients

$$|V_{eN}|^2 = 1.5 \ (2.5) \ [5] \times 10^{-5}, \qquad |V_{\mu N}|^2 = 3.2 \times 10^{-3}, \qquad |V_{\tau N}|^2 = 6.2 \times 10^{-3}, \tag{2.13}$$

JHEP02(2015)072

corresponding to a total neutrino width of

$$\Gamma_N = 0.303\ (1.50)\ [12.3]\ \text{GeV}. \tag{2.14}$$

As $\Gamma_t/m_N \approx 0.1\%-1\%$, the heavy neutrino resonance is very narrow and application of the narrow width approximation (NWA) is justified. For $S_{\ell\ell}$, these mixing parameters imply

$$S_{ee} = 2.4\ (6.6)\ [26] \times 10^{-8} \quad \text{for} \quad m_N = 300\ (500)\ [1000]\ \text{GeV} \tag{2.15}$$

$$S_{e\mu} = S_{\mu e} = 5.1\ (8.5)\ [17] \times 10^{-6} \quad \text{for} \quad m_N = 300\ (500)\ [1000]\ \text{GeV} \tag{2.16}$$

$$S_{\mu\mu} = 1.1 \times 10^{-3} \quad \text{for} \quad m_N \in [100, 1000]\ \text{GeV} \tag{2.17}$$

Though the bound on $|V_{eN}|$ varies with m_N, $S_{\mu\mu}$ changes at the per mil level over the masses we investigate and is taken as constant. The allowed sizes of $S_{e\mu}$, $S_{\mu\mu}$, and $S_{\tau\ell}$ demonstrate the complementarity to searches for L-violation at $0\nu\beta\beta$ experiments afforded by hadron colliders. To make an exact comparison with ref. [29], we also consider the bound [44, 45]

$$S_{\mu\mu} \approx \frac{|V_{\mu N}|^4}{|V_{\mu N}|^2} = |V_{\mu N}|^2 = 6 \times 10^{-3} \tag{2.18}$$

However, bare results, which are mixing-independent, are presented wherever possible.

2.2 N production via the Drell-Yan process at NNLO

Before presenting the production cross sections, it is informative to understand the available parton luminosities (Φ_{ij}) as defined in eq. (2.5). We show $\Phi_{q\overline{q}'}$ versus $\sqrt{\tau}$ for $q\overline{q}'$ annihilation summing over light quarks (u, d, c, s) by the solid (black) curves in figures 3(a) and 3(b) for the 14 TeV LHC and 100 TeV VLHC, respectively. The upper horizontal axis labels the partonic c.m. energy $\sqrt{\hat{s}}$. As expected, at a fixed $\sqrt{\hat{s}}$ the DY luminosity at 100 TeV significantly increases over that at 14 TeV. At $\sqrt{\hat{s}} \approx 500$ GeV (2 TeV), the gain is a factor of 600 (1.8×10^3), and the discovery potential of heavy Majorana neutrinos is greatly expanded. Luminosity ratios with respect to $\Phi_{q\overline{q}'}$ are given in figure 3(c) and 3(d), and will be discussed when appropriate.

Cross sections for resonant N production via the charged current DY process in eq. (1.2) and shown in figure 1 are calculated with the usual helicity amplitudes at the LO α^2. Monte Carlo integration is performed using CUBA [75]. Results are checked by implementing the heavy Majorana neutrino model into FeynRules 2.0.6 [76, 77] and MG5_aMC@NLO 2.1.0 [78] (MG5). For simplicity, percent-level contributions from off-diagonal Cabbibo-Kobayashi-Maskawa (CKM) matrix elements are ignored and the diagonal elements are taken to be unity. SM inputs $\alpha^{\overline{\text{MS}}}(M_Z)$, M_Z, and $\sin^2_{\overline{\text{MS}}}(\theta_W)$ are taken from the 2012 Particle Data Group (PDG) [79].

We estimate the 14 and 100 TeV pp NNLO K-factor[1] by using FEWZ 2.1 [80, 81] to compute the equivalent quantity for the SM process

$$pp \to W^* \to \mu^\pm \nu, \tag{2.19}$$

[1]The N^nLO K-factor is defined as $K = \sigma^{N^nLO}(N\ell)/\sigma^{LO}(N\ell)$, where $\sigma^{N^nLO}(N\ell)$ is the N^{n}LO-corrected cross section and $\sigma^{LO}(N\ell)$ is the lowest order ($n = 0$), or Born, cross section.

JHEP02(2015)072

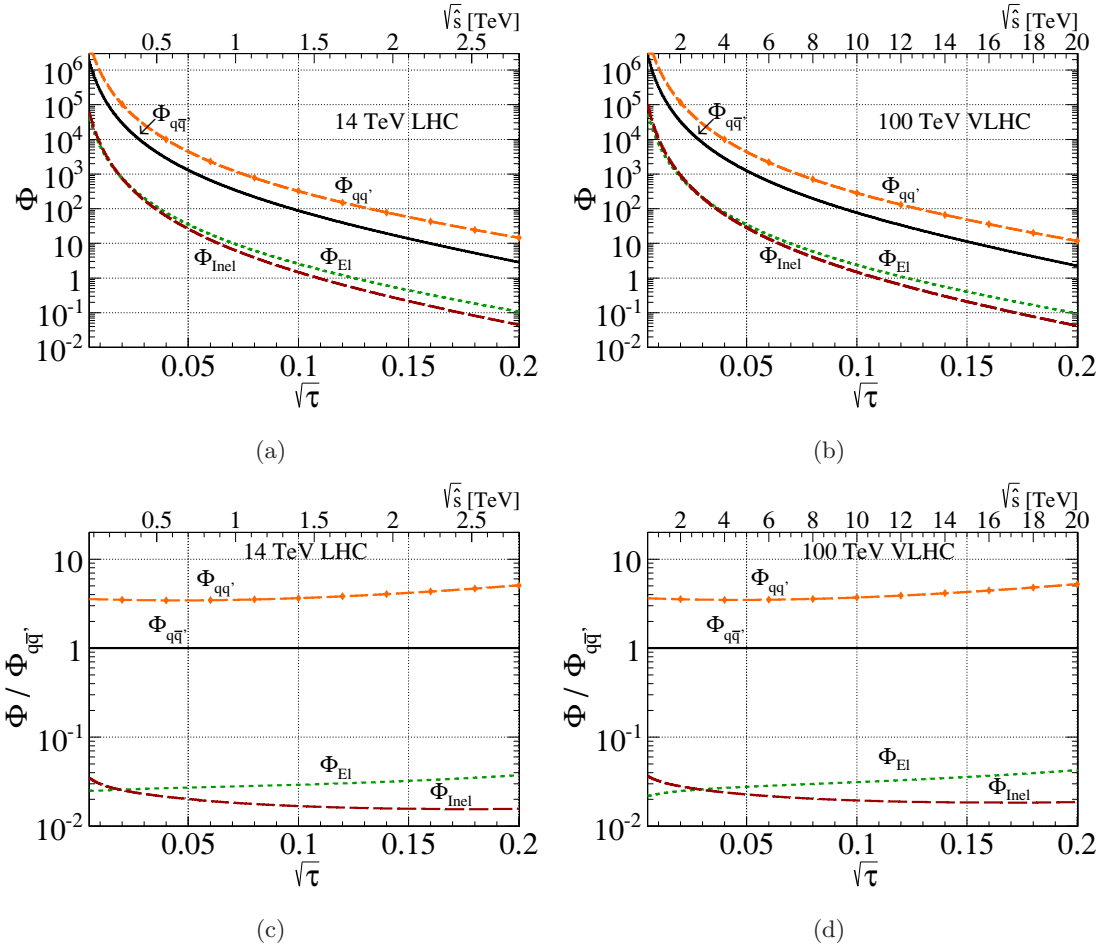

Figure 3. Parton luminosities for (a) at 14 TeV and (b) 100 TeV for the DY (solid), elastic (dot), inelastic (dash), and DIS (dash-diamond) $N\ell X$ processes; ratio of parton luminosities to the DY luminosity in (c) and (d).

$\sqrt{\hat{s}^{\min}}$	14 TeV LO [pb]	NNLO [pb]	K	100 TeV LO [pb]	NNLO [pb]	K
100 GeV	152	209	1.38	1150	1420	1.23
300 GeV	1.54	1.90	1.23	17.0	25.6	1.50
500 GeV	0.248	0.304	1.22	3.56	4.97	1.40
1 TeV	17.0 $\times 10^{-3}$	20.5 $\times 10^{-3}$	1.20	0.380	0.485	1.28

Table 1. LO and NNLO cross sections for $pp \to W^* \to \mu^{\pm}\nu$ at 14 and 100 TeV with successive invariant mass cuts using MSTW2008LO and NNLO PDF Sets.

and impose only an minimum invariant mass cut, $\sqrt{\hat{s}^{\min}}$. Because LO $N\ell$ production and eq. (2.19) are identical DY processes (up mass effects) with the same color structure, K-factors calculated with a fixed $\hat{s}$ are equal.

JHEP02(2015)072

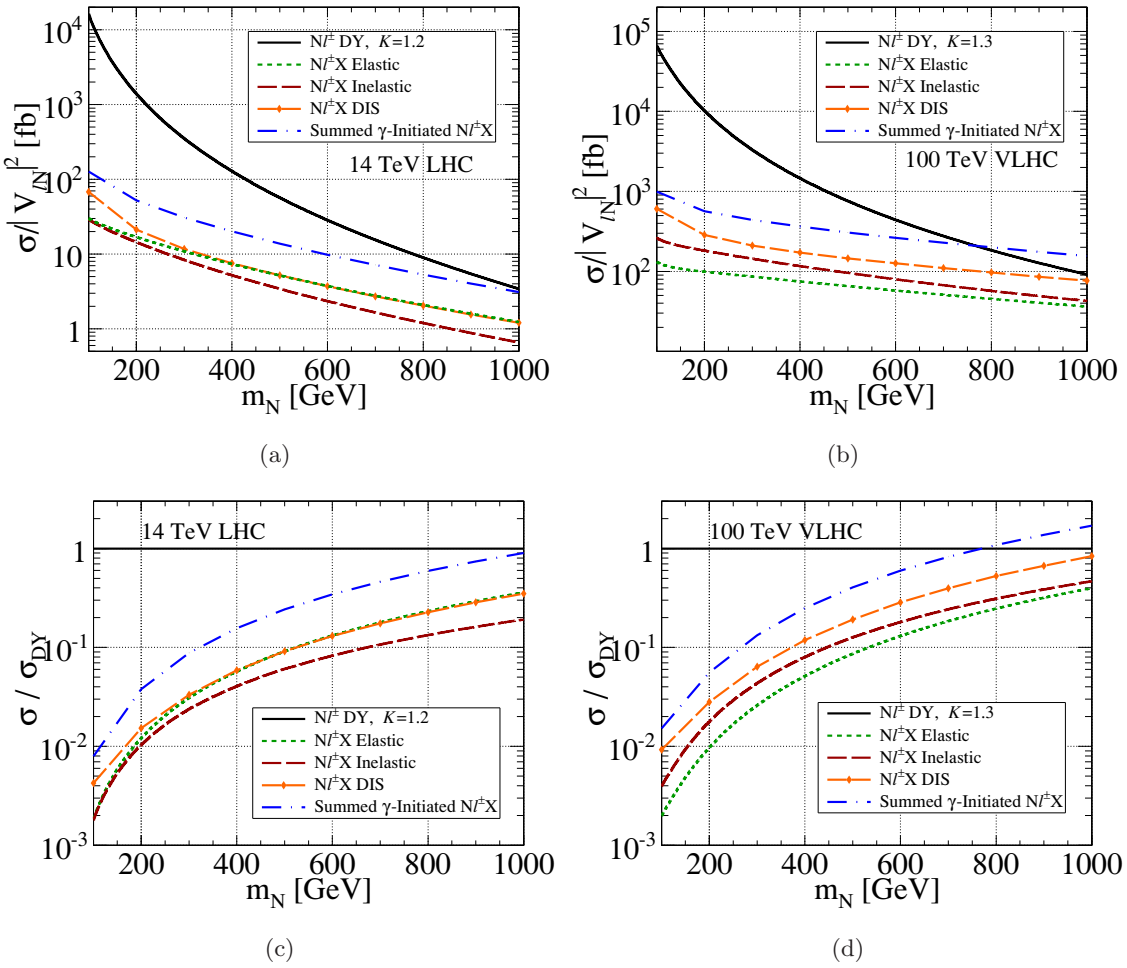

Figure 4. (a) 14 TeV LHC (b) 100 TeV VLHC $N\ell X$ cross section, divided by $|V_{\ell N}|^2$, as a function of the N mass for the NNLO DY (solid), elastic (dot), inelastic (dash), DIS (dash-diamond), and summed γ-initiated (dash-dot) processes. (c,d) Ratio of cross sections relative to NNLO DY rate.

Table 1 lists[2] the LO and NNLO cross sections as well as the NNLO K-factors for several representative values of $\sqrt{\hat{s}^{\min}}$. At $\sqrt{\hat{s}^{\min}} = 1$ TeV, the QCD-corrected charged current rate can reach tens (several hundreds) of fb at 14 (100) TeV. Over the range from $\sqrt{\hat{s}^{\min}} = 100$ GeV $-$ 1 TeV,

$$K = 1.20 - 1.38 \quad \text{at 14 TeV}, \tag{2.20}$$

$$= 1.23 - 1.50 \quad \text{at 100 TeV}. \tag{2.21}$$

This agrees with calculations for similar DY processes [82, 83]. We see that the higher order QCD corrections to the DY channel are quite stable, which will be important for our discussions in section 2.3. Throughout the study, independent of neutrino mass, we apply

[2] As no NNLO CTEQ6L PDF set exists, we have adopted the MSTW2008 series to obtain a self-consistent estimate of the NNLO K-factor.

JHEP02(2015)072

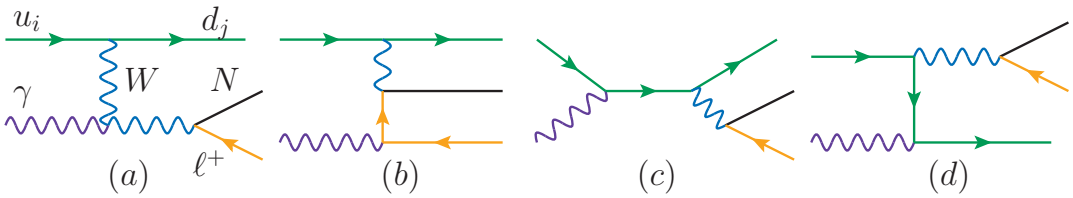

Figure 5. Feynman diagrams for photon-initiated process $q\gamma \to N\ell^\pm q'$.

to the DY-process a K-factor of

$$K = 1.2\ (1.3) \quad \text{for} \quad 14\ (100)\ \ \text{TeV}. \tag{2.22}$$

Including the QCD K-factor, we show the NNLO total cross sections [called the "bare cross section σ_0" by factorizing out $|V_{\ell N}|^2$ as defined in eq. (2.7)] as a function of heavy neutrino mass in figures 4(a) and 4(b) for the 14-TeV LHC and 100-TeV VLHC, respectively. The curves are denoted by the (black) solid lines. Here and henceforth, we impose the following basic acceptance cuts on the transverse momentum and pseudorapidity of the charged leptons for 14 (100) TeV,

$$p_T^\ell > 10\ (30)\ \text{GeV}, \quad |\eta^\ell| < 2.4\ (2.5). \tag{2.23}$$

The motive to include these cuts is two-fold. First, they are consistent with the detector acceptance for our future simulations and the definition of "fiducial" cross section. Second, they serve as kinematical regulators for potential collinear singularities, to be discussed next. The p_T and η criteria at 100 TeV follow the 2013 Snowmass benchmarks [84].

2.3 Photon-initiated processes

After the dominant DY channel, VBF via $W\gamma$ fusion, as introduced in eq. (2.2), presents a promising additional contribution to the heavy N production. We do not make any approximation for the initial state W and treat its radiation off the light quarks with exact matrix element calculations. In fact, we consistently treat the full set of diagrams, shown in figure 5, for the photon-initiated process at order α^3

$$q\ \gamma \to N\ \ell^\pm\ q'. \tag{2.24}$$

Obviously, diagrams figure 5(c) and (d) do not add to $W\gamma$ fusion and are just small QED corrections.[3] Diagram figure 5(b) involves a massless t-channel charged lepton. The collinear pole is regularized by the basic acceptance cuts in eq. (2.23). What is non-trivial, however, is how to properly treat initial-state photons across the different sources depicted in figure 2. We now discuss the individual channels in detail.

[3]Diagram 5(d) involves a collinear singularity from massless quark splitting. It is unimportant for our current consideration since its contribution is simply a QED correction to the quark PDF. For consistency and with little change to our results, $\Lambda_\gamma^{\rm DIS} = 15$ GeV [defined in eq. (2.32)] is applied as a regulator.

JHEP02(2015)072

2.3.1 Elastic scattering: intact final-state nucleons

Here and henceforth, the virtuality for the incoming photon in $W\gamma$ fusion is denoted as $Q_\gamma > 0$. In the collinear limit that results in momentum transfers on the order of the proton mass or less, $Q_\gamma^2 \lesssim m_p^2$, initial-state photons are appropriately described as massless radiation by an elastic proton, i.e., does not break apart and remains as an on-shell nucleon, as indicated in figure 2(a). To model this, we use the "Improved" Weizsäcker-Williams approximation [49] and factorize the photon's collinear behavior into a structure function of the proton to obtain the elastic photon PDF $f_{\gamma/p}^{\rm El}$. In eq. (2.3), this entails replacing one $f_{i/p}$ with $f_{\gamma/p}^{\rm El}$:

$$f_{i/p}(\xi, Q_f^2) \to f_{\gamma/p}^{\rm El}(\xi). \tag{2.25}$$

The expression for $f_{\gamma/p}^{\rm El}$, given in appendix A, is dependent on a cutoff scale $\Lambda_\gamma^{\rm El}$, above which the description of elastic $p \to \gamma$ emission starts to break down. Typically, the scale is taken to be $\mathcal{O}(m_p - 2\text{ GeV})$ [49, 54, 55, 61–65] but should be insensitive to small variations if an appropriate scale is chosen. Based on analysis of ep scattering at low Q_γ [85], we take

$$\Lambda_\gamma^{\rm El} = \sqrt{1.5\text{ GeV}^2} \approx 1.22\text{ GeV}. \tag{2.26}$$

The scale dependence associated with $\Lambda_\gamma^{\rm El}$ is discussed in section 2.5.

In figure 3, the elastic luminosity spectrum ($\Phi_{\rm El}$) is denoted by the (green) dot line. For the range studied, $\Phi_{\rm El}$ is roughly $2-4\%$ of the $q\bar{q}'$ DY luminosity at 14 and 100 TeV.

We calculate the matrix element for the diagrams in figure 5 in the same manner as the DY channel. The results are checked with MG5 using the elastic, asymmetric $p\gamma$ beam mode. In figures 4(a) and 4(b), we plot the bare cross section for the elastic process, denoted by a (green) dot line, as a function of neutrino mass. The rate varies between $1-30$ $(40-100)$ fb at 14 (100) TeV for $m_N = 100\,\text{GeV}-1\,\text{TeV}$. As seen in figures 4(c) and 4(d), where the cross sections are normalized to the DY rate, it reaches about 30 (40)% of the DY rate for large m_N.

2.3.2 Inelastic scattering: collinear photons from quarks

For momentum transfers above the proton mass, the parton model is valid. When this configuration coincides with the collinear radiation limit, initial-state photons are appropriately described as being radiated by quark partons. To model a quark splitting to a photon, we follow the methodology of ref. [57] and use the (original) Weizsäcker-Williams approximation [86, 87] to obtain the inelastic photon PDF $f_{\gamma/p}^{\rm Inel}$. Unlike the elastic case, factorization requires us to convolve about a splitting function. The inelastic $N\ell^\pm X$ cross section is obtained by making the replacement in eq. (2.3)

$$f_{i/p}(\xi, Q_f^2) \to f_{\gamma/p}^{\rm Inel}(\xi, Q_\gamma^2, Q_f^2), \tag{2.27}$$

$$f_{\gamma/p}^{\rm Inel}(\xi, Q_\gamma^2, Q_f^2) = \sum_j \int_\xi^1 \frac{dz}{z}\, f_{\gamma/j}(z, Q_\gamma^2)\, f_{j/p}\left(\frac{\xi}{z}, Q_f^2\right), \tag{2.28}$$

where $f_{\gamma/j}$ is the Weizsäcker-Williams $j \to \gamma$ distribution function, with Q_γ and Q_f being the factorization scales for the photon and quark distributions, respectively. The summation is over all charged quarks. Details regarding eq. (2.28) can be found in appendix B.

JHEP02(2015)072

Clearly, the scale for the photon momentum transfer should be above the elastic bound $Q_\gamma \geq \Lambda_\gamma^{\rm El}$. What is not clear, however, is how high we should evolve Q_γ. If we crudely consider the total inclusive cross section, we could simply choose the kinematical upper limit $Q_\gamma^2 \approx Q_f^2 \approx \hat{s}/4$ or $\hat{s}/4 - m_N^2$, which is a quite common practice in the literature [57]. However, we do not consider this a satisfactory treatment. Well below the kinematical upper limit, the photon virtuality Q_γ becomes sufficiently large so that the collinear photon approximation as in figure 5 breaks down. Consequently, "deeply inelastic scattering" (DIS), as in figure 6, becomes the dominant feature. Thus, a more reasonable treatment is to introduce an upper limit for the inelastic process $\Lambda_\gamma^{\rm DIS}$, above which a full DIS calculation of figure 6 should be applied. We adopt the following scheme

$$Q_\gamma = \Lambda_\gamma^{\rm DIS} = \begin{cases} 15 \text{ GeV} & \text{for } 14 \text{ TeV} \\ 25 \text{ GeV} & \text{for } 100 \text{ TeV} \end{cases} \tag{2.29}$$

Sensitivity to variations $\Lambda_\gamma^{\rm DIS}$ are discussed in section 2.5.

Consistent with $\Phi_{ij}(\tau)$ in eq. (2.5), we define the inelastic γq parton luminosity $\Phi_{\rm Inel}$ to be

$$\Phi_{\rm Inel}(\tau) = \int_\tau^1 \frac{d\xi}{\xi} \int_{\tau/\xi}^1 \frac{dz}{z} \sum_{q,q'} \left[f_{q/p}(\xi) f_{\gamma/q'}(z) f_{q'/p}\left(\frac{\tau}{\xi z}\right) + f_{q/p}\left(\frac{\tau}{\xi z}\right) f_{\gamma/q'}(z) f_{q'/p}(\xi) \right]. \tag{2.30}$$

In figure 3, we give the $\Phi_{\rm Inel}$ spectrum as a function of $\sqrt{\tau}$, denoted by the (red) dash curve, for 14 and 100 TeV. For the range investigated, $\Phi_{\rm Inel}$ ranges between $2-4\%$ of the DY luminosity. Compared to its elastic counterpart, the smallness of the inelastic luminosity is attributed the limited Q_γ^2 evolution.

The inelastic matrix element is identical to the elastic case. In figures 4(a) and 4(b), we show the bare cross section for the inelastic process, denoted by the (red) dash line, as a function of the neutrino mass. The rate varies between $0.7 - 30$ $(40 - 260)$ fb at 14 (100) TeV for $m_N = 100$ GeV $- 1$ TeV. As seen in figures 4(c) and 4(d), where the cross sections are normalized to the DY rate, it reaches about 10 (50)% of the DY rate at large m_N.

2.3.3 Deeply inelastic scattering: high p_T quark jet

As discussed in the previous section, at a sufficiently large momentum transfer the collinear photon description breaks down and the associated final-state quark emerges as an observable jet. The electroweak process at α^4

$$q_1\ q_2 \to N\ \ell^\pm\ q_1'\ q_2'. \tag{2.31}$$

becomes DIS, as shown by the Feynman diagrams in figure 6. The top row of figure 6 can be identified as the DIS analog of those diagrams in figure 5. Again, the first two diagrams represent the $W\gamma$ fusion with collinear log-enhancement from t-channel W exchange. At these momentum transfers, the WZ fusion channel [26] turns on but is numerically smaller; see figure 6, bottom row, first diagram. The center row and two bottom-rightmost diagrams in figure 6 represent on-shell W/Z production at α^3 with subsequent $W/Z \to q\overline{q}'$ decay.

JHEP02(2015)072

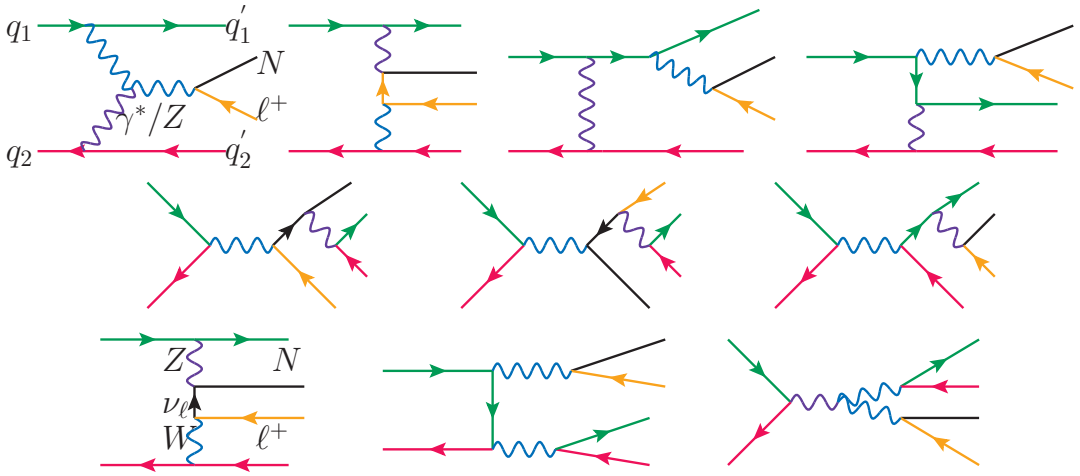

Figure 6. Feynman diagrams for the DIS process $q_1 q_2 \to N\ell^\pm q_1' q_2'$.

Those processes, however, scale as $1/\hat{s}$ and are not log-enhanced. A subset of these last diagrams also represent higher-order QED corrections to the DY process.

To model DIS, we use MG5 and simulate eq. (2.31) at order α^4. We impose[4] at the generator level a minimum on momentum transfers between initial-state and final-state quarks

$$\min_{i,j=1,2} \sqrt{|(q_i - q_j')^2|} > \Lambda_\gamma^{\text{DIS}}. \tag{2.32}$$

This requirement serves to separate the elastic and inelastic channels from DIS. Sensitivity to this cutoff is addressed in section 2.5.

In figure 3, we show the quark-quark parton luminosity spectrum $\Phi_{\text{qq}'}$, the source of the DIS processes, and represented by the (orange) dash-diamond curves. Though possessing the largest parton luminosity, the channel must overcome its larger coupling and phase space suppression. At 14 and 100 TeV, $\Phi_{\text{qq}'}$ ranges $3-5$ times larger than $\Phi_{\text{q}\bar{\text{q}}'}$. The difference in size between $\Phi_{\text{qq}'}$ and $\Phi_{\text{El (Inel)}}$ is due to the additional coupling α_{EM} in $f_{\gamma/p}^{\text{El (Inel)}}$.

In figures 4(a) and 4(b), we plot bare cross section as in eq. (2.7), denoted by the (orange) dash-diamond curve. In figures 4(c) and 4(d), the same curves are normalized to the DY rate. At 14 (100) TeV, the cross section ranges from $1-60$ $(80-500)$ fb, reaching about 35% (80%) of the DY rate.

To compare channels, we observe that the DIS (elastic) process increases greatest (least) with increasing collider energies. This is due to the increase likelihood for larger momentum transfers in more energetic collisions. A similar conclusion was found for elastic and inelastic $\gamma\gamma$ scattering at the Tevatron and LHC [59].

[4]For consistency, we also require the lepton cuts given in eq. (2.23) and a jet separation $\Delta R_{jj} > 0.4$ to regularize irrelevant $\gamma^* \to q\bar{q}$ diagrams, where $\Delta R \equiv \sqrt{\Delta\phi^2 + \Delta\eta^2}$ with $y = \eta \equiv -\log[\tan(\theta/2)]$ in the massless limit.

JHEP02(2015)072

$\sigma_{14\text{ TeV LHC}}/\lvert V_{\ell N}\rvert^2$ [fb]	$m_N = 300$ GeV	$m_N = 500$ GeV	$m_N = 1$ TeV
$pp \to N\ell^\pm$ LO DY $[K = 1.2]$	293 (352)	47.3 (56.8)	2.87 (3.44)
$pp \to N\ell^\pm X$ Elastic	10.8971	5.16756	1.23693
$pp \to N\ell^\pm X$ Inelastic	8.32241	3.44245	0.65728
$pp \to N\ell^\pm X$ DIS	11.7	5.19	1.21
$\sigma_{\gamma-\text{Initiated}}/\sigma_{\text{DY}}^{K=1.2}$	0.09	0.24	0.90
$\sigma_{100\text{ TeV VLHC}}/\lvert V_{\ell N}\rvert^2$ [fb]	$m_N = 300$ GeV	$m_N = 500$ GeV	$m_N = 1$ TeV
$pp \to N\ell^\pm$ LO DY $[K = 1.3]$	2540 (3300)	583 (758)	70.5 (91.6)
$pp \to N\ell^\pm X$ Elastic	85.8	65.5	36.4
$pp \to N\ell^\pm X$ Inelastic	144	96.0	42.7
$pp \to N\ell^\pm X$ DIS	210	145	76.7
$\sigma_{\gamma-\text{Initiated}}/\sigma_{\text{DY}}^{K=1.3}$	0.13	0.40	1.7

Table 2. Total cross sections of various $pp \to N\ell^\pm X$ channels for representative values of m_N. Minimal acceptance cuts as in eqs. (2.23) have been applied.

2.3.4 Total neutrino production from γ-initiated processes

The total heavy neutrino production cross section from γ-initiated processes may be obtained by summing the elastic, inelastic, and DIS channels [57, 59]:

$$\sigma_{\gamma-\text{Initiated}}(N\ell^\pm X) = \sigma_{\text{El}}(N\ell^\pm X) + \sigma_{\text{Inel}}(N\ell^\pm X) + \sigma_{\text{DIS}}(N\ell^\pm X), \tag{2.33}$$

We plot eq. (2.33) as a function of m_N in figures 4(a) and 4(b) at 14 and 100 TeV, denoted by the (blue) dash-dot curve. In figures 4(c) and 4(d), the same curves are normalized to the DY rate. For $m_N = 100$ GeV-1 TeV, the total rate spans $3-100$ $(150-1000)$ fb at 14 (100) TeV, reaching about 90 (110)% of the DY rate at large m_N. We find that the $W\gamma$ fusion represents the largest heavy neutrino production mechanism for $m_N > 1$ TeV (770) GeV at 14 (100) TeV. We expect for increasing collider energy this crossover will occur earlier at lighter neutrino masses. Cross sections for representative values of m_N for all channels at 14 and 100 TeV are given in table 2.

Before closing the discussion for the heavy N production at hadron colliders, an important remark is in order. We have taken into account the *inclusive* QCD correction at NNLO as a K-factor. In contrast, ref. [36] included only the tree-level process at order $\alpha^2\alpha_s^2$ and α^4

$$pp \to N\ell^\pm jj. \tag{2.34}$$

When calculating the exclusive $N\ell^\pm jj$ cross section, kinematical cuts of $p_{Tj} > 10$ GeV and $\Delta R_{jj} > 0.4$ were applied to regularize the cross section. For $m_N = 300$ GeV, the exclusive cross section was found to exceed the LO DY channel at 14 TeV, whereas we find that the NNLO correction to the inclusive cross section is only 20% with DIS contributing 3%. More recently [60], the tree-level rate for $N\ell j$ with $p_T^j > 30$ GeV was calculated to be 80% of the LO DY rate at $m_N = 500$ GeV; at NNLO, we find the inclusive correction to be

JHEP02(2015)072

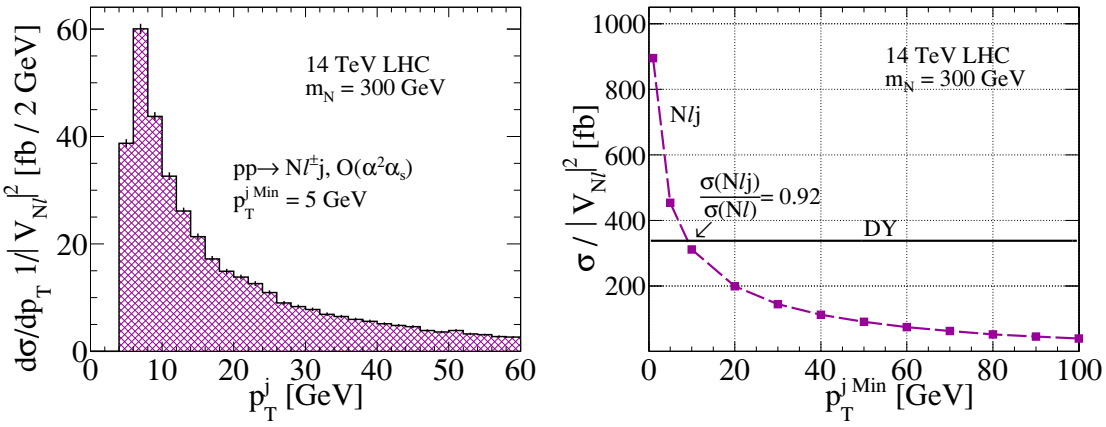

(a) (b)

Figure 7. (a) The tree-level differential cross section for $N\ell^{\pm}j$ at $\alpha^2\alpha_{\rm s}$ with respect to p_T^j; (b) Integrated cross section $\sigma(N\ell^{\pm}j)$ versus the minimum p_T^j cutoff. The solid line denotes the LO DY rate.

only 20%. We attribute these discrepancies to their too low a p_T^j cut that overestimate the contribution of initial-state radiation based on a tree-level calculation.

To make the point concrete, we consider the tree-level QCD correction to the DY process at order $\alpha^2\alpha_{\rm s}$

$$p\ p \to N\ \ell^{\pm}\ j, \tag{2.35}$$

where the final-state jet originates from an initial-state quark or gluon. MG5 is used to simulated eq. (2.35). In figure 7(a), the differential cross section of p_T^j is shown for a minimal p_T at 5 GeV. The singularity at the origin is apparent. In figure 7(b), the 14 TeV LHC cross section as a function of minimum p_T cut on the jet is presented. A representative neutrino mass of $m_N = 300$ GeV is used; no additional cut has been imposed. At $p_T^{j\,\rm min} = 10$ GeV, as adopted in ref. [36], the $N\ell j$ rate is nearly equal to the DY rate, well above the NNLO prediction for the inclusive cross section [48].

2.4 Kinematic features of N production with jets at 14 TeV

To explore the kinematic distributions of the inclusive neutrino production, we fix $\sqrt{s} =$ 14 TeV and $m_N = 500$ GeV. At 100 TeV, we observe little change in the kinematical features and our conclusions remain the same. The most notable difference, however, is a broadening of rapidity distributions. This is due an increase in longitudinal momentum carried by the final states, which follows from the increase in average momentum carried by initial-state partons. For $m_N \geq 100$ GeV, we observe little difference from the 500 GeV case we present. Throughout this study, jets are ranked by p_T, namely, the jet with the largest (smallest) p_T is referred to as hardest (softest).

In figure 8, we plot the (a) p_T and (b) η distributions of the hardest jet in p_T produced in association with N for the various $W\gamma$ fusion channels. Also shown are (c) p_T and (d) η distributions of the sub-leading jet for the DIS channel. For the hardest jet, we observe a plateau at $p_T \sim M_W/2$ and a rapidity concentrated at $|\eta| \sim 3.5$, suggesting dominance

JHEP02(2015)072

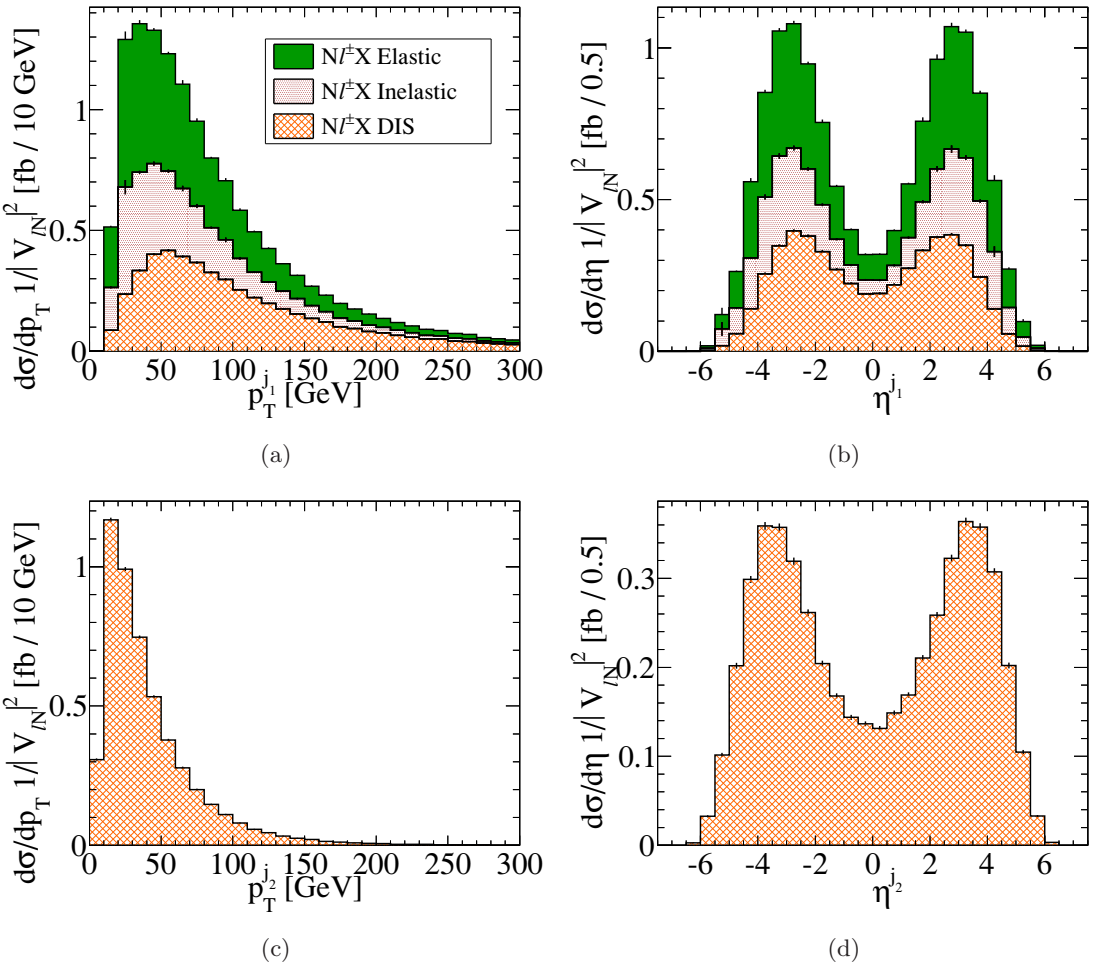

(a) (b) (c) (d)

Figure 8. Stacked (a) p_T and (b) η differential distributions, divided by $|V_{\ell N}|^2$, at 14 TeV LHC of the leading jet in the elastic (solid fill), inelastic (dot fill), and DIS (crosshatch fill) processes. (c) p_T and (d) η of the sub-leading jet in DIS.

of t-channel W boson emission. For the soft jet, we observe a rise in cross section at low p_T and a rapidity also concentrated at $|\eta| \sim 3.5$, indicating t-channel emission of a massless vector boson. We conclude that VBF is the driving contribution γ-initiated heavy neutrino production.

In figure 9, we plot the (a) p_T and (b) η distributions of the charged lepton produced in association with N for all channels contributing to $N\ell$ production. Also shown are the (c) p_T and (d) y distribution of N. For both leptons, we observed a tendency for softer p_T and broader rapidity distributions in γ-initiated channels than in the DY channel. As DY neutrino production proceeds through the s-channel, N and ℓ possess harder p_T than the γ-initiated states, which proceed through t-channel production and are thus more forward.

2.5 Scale dependence

For the processes under consideration, namely DY and $W\gamma$ fusion, there are two factorization scales involved: Q_f and Q_γ. They characterize typical momentum transfers of the

JHEP02(2015)072

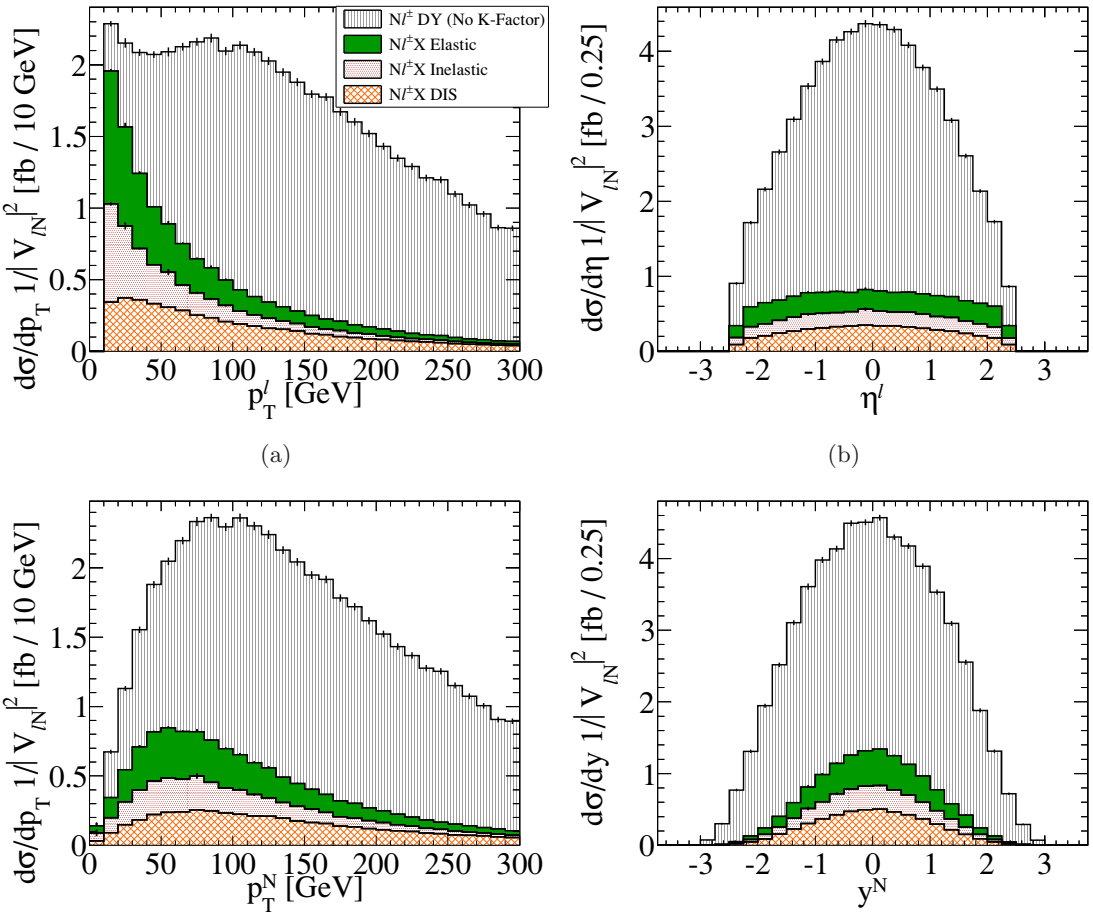

(a) (b) (c) (d)

Figure 9. Stacked (a) p_T and (b) η differential distributions at 14 TeV LHC of the charged lepton produced in association with N for the DY (line fill), elastic, inelastic and DIS processes. (c) p_T and (d) y of N for the same processes. Fill style and normalization remain unchanged from figure 8.

Scale Parameter	Default at 14 (100) TeV	Lower	Upper	Variation at 14 (100) TeV
$\Lambda_\gamma^{\rm El}$ [Eq. (2.25)]	1.22 GeV	m_p	2.3 GeV	$\mathcal{O}(10\%)$ (12%)
		m_p	5 GeV	$\mathcal{O}(22\%)$ (28%)
$\Lambda_\gamma^{\rm DIS}$ [Eq. (2.29)]	15 GeV (25 GeV)	5 GeV	50 GeV	$\mathcal{O}(10\%)$ (15%)
		5 GeV	150 GeV	$\mathcal{O}(18\%)$ (27%)
$Q_f^{\rm DY}$ [Eq. (2.3)]	$\sqrt{\hat{s}}/2$	$m_N/2$	$\sqrt{\hat{s}}$	$\mathcal{O}(10\%)$ (5%)
$Q_f^{\rm DIS}$ [Eq. (2.3)]	$\sqrt{\hat{s}}/2$	$m_N/2$	$\sqrt{\hat{s}}$	$\mathcal{O}(15\%)$ (8%)

Table 3. Summary of scale dependence in $N\ell^\pm X$ production at 14 TeV and 100 TeV.

physical processes. For the γ-initiated channels, we separate the contributions into three regimes using $\Lambda_\gamma^{\rm El}$ and $\Lambda_\gamma^{\rm DIS}$. Though the quark parton scale Q_f is present in all channels, we assume it to be near m_N and set it as in eq. (2.6).

JHEP02(2015)072

To quantify the numerical impact of varying these scales, each relevant cross section as a function of m_N is computed with one scale varied while all other scales are held at their default values. The test ranges are taken as

$$\begin{aligned} m_p \leq \Lambda_\gamma^{\rm El} \leq 5 \text{ GeV}, \\ 5 \text{ GeV} \leq Q_\gamma = \Lambda_\gamma^{\rm DIS} \leq 150 \text{ GeV}, \\ \frac{m_N}{2} \leq Q_f \leq \sqrt{\hat{s}}, \end{aligned} \tag{2.36}$$

In figure 10, we plot the variation band in each production channel cross section due to the shifting scale. For a given channel, rates are normalized to the cross section using the default scale choices, as discussed in the previous sections and summarized in the first column of table 3. High-(low-) scale choices are denoted by a solid line with right-side (upside-down) up triangles.

For the 14 TeV LO DY process, we observe in figure 10(a) maximally a 9% upward (7% downward) variation for the range of m_N investigated. Below $m_N \approx 300$ GeV, the default scale scheme curve is below (above) the high (low) scale scheme curve. The trend is reversed for above $m_N \approx 300$ GeV. At 100 TeV, the crossover point shifts to much higher values of m_N. Numerically, we observe a smaller scale dependence at the 5% level.

In figure 10(b), we plot scale variation associated with the factorization scale Q_f for DIS. Maximally, we observe a 16% upward (8% downward) shift. We observe that the crossover between the high and low scale schemes now occurs at $m_N \lesssim 100$ GeV. This is to be expected as $\hat{s}$ for the 4-body DIS at a fixed neutrino mass is much larger than that for the 2-body DY channel. Similarly, as $\sqrt{\hat{s}}$ and m_N are no longer comparable, as in the DY case, an asymmetry between the high- and low-scale scheme curves emerges. At 100 TeV, we observe a smaller dependence at the 10% level.

In figure 10(c), we show the dependence on $\Lambda_\gamma^{\rm El}$ in the elastic (dot) and inelastic (dash) channels, as well as the sum of the two channels (dash-dot). For the elastic channel we find very small dependence on $\Lambda_\gamma^{\rm El}$ between m_p and 5 GeV, with the analytical expression for $f_{\gamma/p}^{\rm El}$ given in appendix A. For the inelastic channel, on the other hand, we find rather large dependence on $\Lambda_\gamma^{\rm El}$ between m_p and 5 GeV. Since $\Lambda_\gamma^{\rm El}$ acts as the regulator of the inelastic channel's collinear logarithm, this large sensitivity is expected; see appendix B for details regarding $f_{\gamma/p}^{\rm Inel}$. We find that the summed rate is slightly more stable. In the region $m_p < \Lambda_\gamma^{\rm El} < 2.3$ GeV, the variation is below the 10% level. Over the entire range studied, this grows to 20%. At 100 TeV, similar behavior is observed and the dependence grows to the 30% level over the whole range.

In figure 10(d), for $m_N = 500$ GeV, we plot the scale dependence on $\Lambda_\gamma^{\rm DIS}$ in the inelastic (dash) and DIS (dash-diamond) channels, as well as the sum of the two channels (dash-dot). Very large sensitivity on the scale is found for individual channels, ranging $40\% - 60\%$ over the entire domain. However, as the choice of $\Lambda_\gamma^{\rm DIS}$ is arbitrary, we expect and observe that their sum is considerably less sensitive to $\Lambda_\gamma^{\rm DIS}$. For $\Lambda_\gamma^{\rm DIS} = 5 - 50$ $(5 - 150)$ GeV, we find maximally a 10% (18%) variation. The stability suggests the channels are well-matched for scales in the range of $5 - 50$ GeV. Results are summarized in table 3.

JHEP02(2015)072

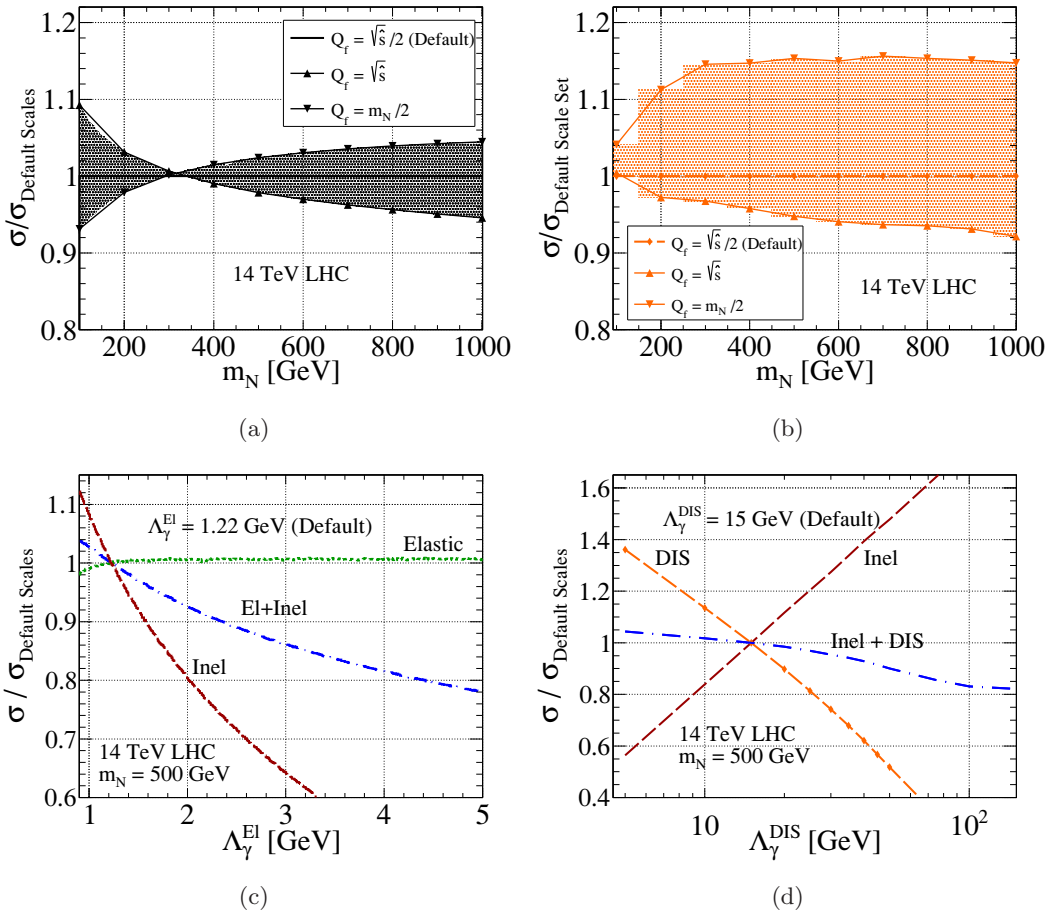

Figure 10. Cross section ratios relative to the default scale scheme, as a function of m_N, for the high-scale (triangle) and low-scale (upside-down triangle) Q_f scheme in (a) DY and (b) DIS. The same quantity as a function of (c) $\Lambda_\gamma^{\rm El}$ in elastic (dot), inelastic (dash), elastic+inelastic (dash-dot) scattering; (d) $\Lambda_\gamma^{\rm DIS}$ in inelastic (dash), DIS (dash-diamond), and inelastic+DIS (dash-dot).

3 Heavy neutrino observability at hadron colliders

3.1 Kinematic features of heavy N decays to same-sign leptons with jets at 100 TeV

We consider at a 100 TeV pp collider charged current production of a heavy Majorana neutrino N in association with $n = 0,\ 1$ or 2 jets, and its decay to same-sign leptons and a dijet via the subprocess $N \to \ell W \to \ell jj$:

$$p\,p \to\ N\,\ell^\pm\ +\ nj \to \ell^\pm\,\ell'^\pm\ +\ (n+2)j, \quad n = 0,\ 1,\ 2. \tag{3.1}$$

Event simulation for the DY and DIS channels was handled with MG5. A NNLO K-factor of $K = 1.3$ is applied to the LO DY channel; kinematic distributions are not scaled by K. Elastic and inelastic channels were handled by extending neutrino production calculations to include heavy neutrino decay. The NWA with full spin correlation was applied. The elastic channel matrix element was again checked with MG5.

JHEP02(2015)072

Detector response was modeled by applying a Gaussian smearing to jets and leptons. For jet energy, the energy resolution is parameterized by [88]

$$\frac{\sigma_E}{E} = \frac{a}{\sqrt{E/\text{ GeV}}} \oplus b, \tag{3.2}$$

with $a = 0.6$ (0.9) and $b = 0.05$ (0.07) for $|\eta| \leq 3.2$ (> 3.2), and where the terms are added in quadrature, i.e., $x \oplus y = \sqrt{x^2 + y^2}$. For muons, the inverse-p_T resolution is parameterized by [88]

$$\frac{\sigma_{1/p_T}}{(1/p_T)} = \frac{0.011 \text{ GeV}}{p_T} \oplus 0.00017. \tag{3.3}$$

We will eventually discuss the sensitivity to the $e^{\pm}\mu^{\pm}$ final state and thus consider electron p_T smearing. For electrons,[5] the p_T resolution is parameterized by [88]

$$\frac{\sigma_{p_T}}{p_T} = 0.66 \times \left(\frac{0.10}{\sqrt{p_T/\text{ GeV}}} \oplus 0.007 \right). \tag{3.4}$$

Both the muon $1/p_T$ and electron p_T smearing are translated into an energy smearing, keeping the polar angle unchanged. We only impose the cuts on the charged leptons as listed in eq. (2.23).

In figure 11, we show the transverse momentum and pseudorapidity distributions of the final-state jets and same-sign dileptons for the processes in eq. (3.1), for $m_N = 500\,\text{GeV}$. Jets originating from N decay are denoted by j_{W_i}, for $i = 1, 2$, and are ranked by p_T ($p_T^{j_{W_1}} > p_T^{j_{W_2}}$). As the three-body $N \to \ell jj$ decay is preceded by the two-body $N \to \ell W$ process, $p_T^{j_W}$ scales like $m_N/4$, as seen in figure 11(a). The jets produced in association with N are denoted by j_3 or j_4, and also ranked by p_T. As VBF drives these channels, we expect j_3 (associated with W^*) and j_4 (associated with γ^*) to scale like $M_W/2$ and $\Lambda_\gamma^{\text{DIS}}$, respectively. In figure 11(b), the η distributions of all final-state jets are shown. We see that j_3 and j_4 are significantly more forward than j_{W1} and j_{W2}, consistent with jets participating in VBF. The high degree of centrality of j_{W1} and j_{W2} follows from the central W decay.

In figures 11(c) and 11(d), we plot the p_T and η distributions of the final-state leptons. The charged lepton produced in association with N is denoted by ℓ_1 and the neutrino's child lepton by ℓ_N. As a decay product, $p_T^{\ell_N}$ scales like $(m_N - M_W)/2$, whereas $p_T^{\ell_1}$ scales as $(\sqrt{\hat{s}} - m_N)/2$. ℓ_1 tends to be soft and more forward in the γ-initiated channels.

3.2 Signal definition and event selection: same-sign leptons with jets

For simplicity, we restrict our study to electrons and muons. We design our cut menu based on the same-sign muon channel. Up to detector smearing effects, the analysis remains unchanged for electrons. A summary of imposed cuts are listed in table 4. Jets and leptons are identified by imposing an isolation requirement; we require

$$\Delta R_{jj} > 0.4, \quad \Delta R_{\ell\ell} > 0.2. \tag{3.5}$$

[5] For this group of exotic searches, the dominant lepton uncertainty stems from p_T mis-measurement. The energy uncertainty is only 1% versus a 20% uncertainty in the electron p_T resolution [88].

JHEP02(2015)072

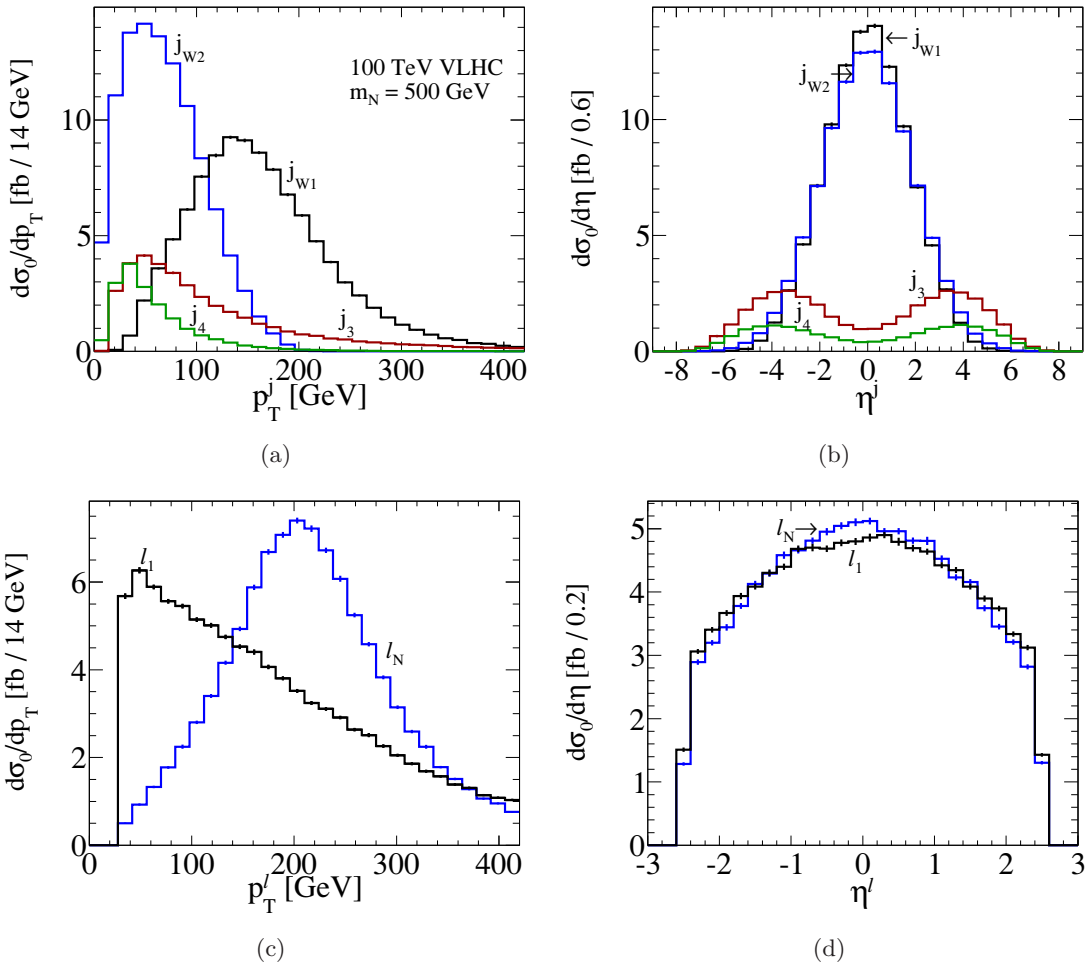

Figure 11. (a) p_T and (b) η differential distributions of the final-state jets for the processes in eq. (3.1), for $m_N = 500$ GeV; (c,d) the same for final-state same-sign dileptons.

Lepton Cuts	Jet Cuts	Other Cuts
$\Delta R_{\ell\ell} > 0.2$ p_T^ℓ ($p_T^{\ell\,\mathrm{Max}}$) > 30 (60) GeV $\lvert\eta^\ell\rvert < 2.5$	$\Delta R_{jj} > 0.4$ p_T^j ($p_T^{j\,\mathrm{Max}}$) > 30 (40) GeV $\lvert\eta^j\rvert < 2.5$ $\lvert M_W^{\mathrm{Candidate}} - M_W\rvert < 20$ GeV $\lvert m_{jjj} - m_t\rvert < 20$ GeV (Veto)	$\Delta R_{\ell j}^{\mathrm{Min}} > 0.6$ $\not{E}_T < 50$ GeV $\lvert m_N^{\mathrm{Candidate}} - m_N\rvert < 20$ GeV

Table 4. Parton-level cuts on 100 TeV $\mu^\pm\mu^\pm jjX$ Analysis.

We define our signal as two muons possessing the same electric charge and at least two jets satisfying the following fiducial and kinematic requirements:

$$|\eta^\ell| < 2.5, \quad p_T^\ell > 30 \text{ GeV}, \quad |\eta^j| < 2.5, \quad p_T^j > 30 \text{ GeV}. \tag{3.6}$$

The bare cross sections [defined by factorizing out $S_{\ell\ell}$ as defined in eq. (2.8)] after cuts listed in eqs. (3.6) and (3.5) and smearing are given in the first row of table 5, for representative masses $m_N = 300,\ 500$, and 1000 GeV. Events with additional leptons are rejected. Events

JHEP02(2015)072

σ_0 [Eq. (2.8)] [fb] \ m_N [GeV]	300	500	1000
Fiducial + Kin. + Smearing [Eq. (3.6)]	281 (41%)	83.9 (45%)	11.6 (28%)
Leading p_T Minimum [Eq. (3.7)]	278 (99%)	83.8 (>99%)	11.6 (>99%)
$\Delta R_{\ell j}$ Separation [Eq. (3.9)]	264 (95%)	79.3 (95%)	10.7 (92%)
$\not{E}_T$ Maximum [Eq. (3.10)]	263 (>99%)	78.1 (99%)	10.1 (95%)
M_W Reco. [Eq. (3.11)]	252 (96%)	74.1 (95%)	9.51 (94%)
m_t Veto [Eq. (3.12)]	251 (99%)	73.5 (99%)	9.42 (99%)
m_N Reco. [Eq. (3.13)]	244 (98%)	64.7 (88%)	7.79 (83%)
Acceptance $[\mathcal{A}] = \sigma_0^{\text{All Cuts}}/\sigma_0^{\text{Fid.+Kin.+Sm.}}$	87%	77%	67%

Table 5. Acceptance rates and percentage efficiencies for the signal $\mu^\pm\mu^\pm jjX$ at 100 TeV VLHC.

with additional jets are kept; we have not tried to utilize the VBF channel's high-rapidity jets. About 30-45% of all $\ell^\pm\ell'^\pm jjX$ events survive these cuts. As learned from figure 11, the η requirement given in ref. [84] considerably reduces selection efficiency. Extending the fiducial coverage to $\eta^{\text{Max}} = 3$ or larger, though technically difficult, can be very beneficial experimentally.

We plot the maximum p_T of jets in figure 12(a) and of charged leptons in figure 12(b), for $m_N = 300,\ 500$ and 1000 GeV. One finds that the $p_T^{j\ \text{Max}}$ scale is $m_N/4$ and is set by the $N \to W \to jj$ chain. For the lepton case, $p_T^{\ell\ \text{Max}}$ is set by the neutrino decay and scales as $m_N/2$. In light of these, we apply the following additional selection cuts to reduce background processes:

$$p_T^{j\ \text{Max}} > 40\ \text{GeV}, \quad p_T^{\ell\ \text{Max}} > 60\ \text{GeV}. \tag{3.7}$$

The corresponding rate is given in the second row of table 5 and we find that virtually all events pass eq. (3.7). As both p_T^{Max} are sensitive to m_N, searches can be slightly optimized by instead imposing the variable cut

$$p_T^{j\ \text{Max}} \gtrsim \mathcal{O}\left(\frac{m_N}{4}\right), \quad p_T^{\ell\ \text{Max}} \gtrsim \mathcal{O}\left(\frac{m_N}{2}\right). \tag{3.8}$$

In each of the several production channels, the final-state charged leptons and jets are widely separated in ΔR; see figure 12(c). With only a marginal effect on the signal rate, we impose the following cut that greatly reduce heavy quarks backgrounds such as $t\bar{t}$ production [27]:

$$\Delta R_{\ell j}^{\text{min}} > 0.6. \tag{3.9}$$

The corresponding rate is given in the third row of table 5. If needed, eq. (3.9) can be set as high as 1.0 and still maintain a high signal efficiency.

In figure 12(d), the separation between the jets in the N decay is shown. For increasing m_N, the separation decreases. This is the result of the W boson becoming more boosted at larger m_N, resulting in more collimated jets. For TeV-scale N, substructure techniques become necessary for optimize event identification and reconstruction. We reserve studying the inclusive same-sign leptons with at least one (fat) jet for a future analysis.

JHEP02(2015)072

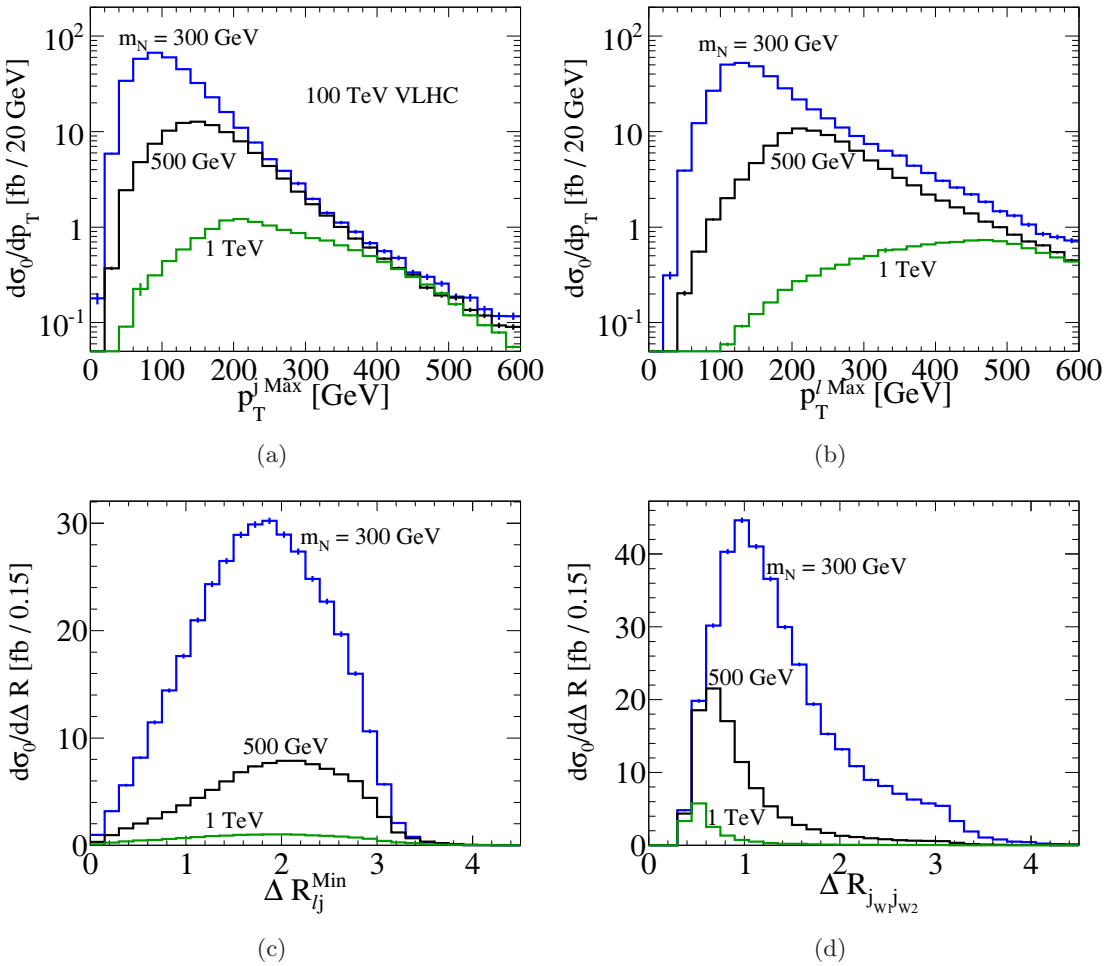

Figure 12. (a) Maximum jet p_T, (b) maximum charged lepton p_T, (c) minimum $\Delta R_{\ell j}$, (d) ΔR_{jW1jW2} distributions for $m_N = 300,\ 500$, and 1000 GeV.

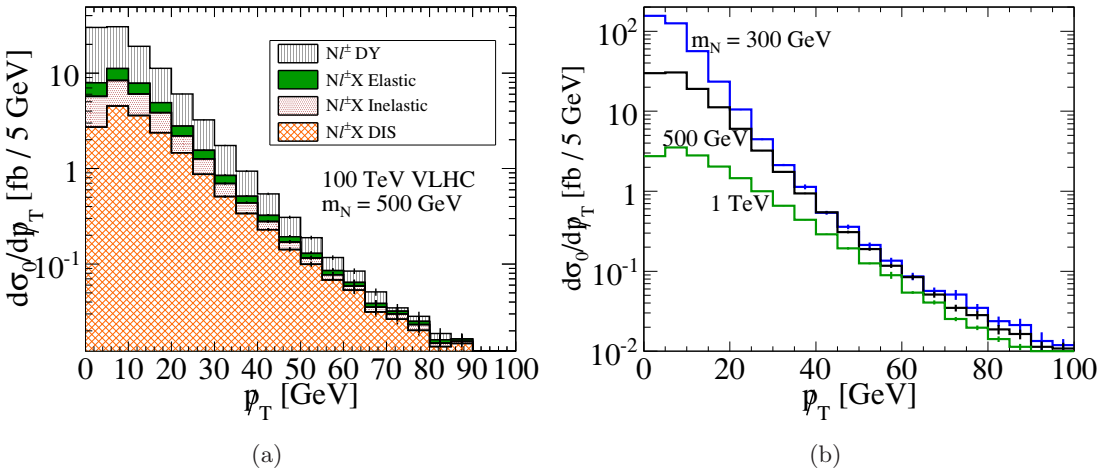

Figure 13. (a) $\not{p}_T$ for individual contributions to $pp \to \ell^{\pm}\ell'^{\pm}jjX$ at $m_N = 500$ GeV. (b) Total $\not{p}_T$ for same m_N as figure 12.

JHEP02(2015)072

For the signature studied here, no light neutrinos are present in the final state. For the heavy neutrino widths listed in eq. (2.14), the decay length $\beta c\tau$ is from $10^{-2} - 1\,\text{fm}$, indicating that N is very short-lived. Thus, there is no source of missing transverse momentum (MET) in the same-sign leptons with $(n+2)j$ aside from detector-level mis-measurements, which are parameterized by eqs. (3.2)–(3.4). With this smearing parameterization, forward (large η) jets are observed with less precision than central (small η) jets. Due to the naturally larger energies associated with forward jets participating in VBF at 100 TeV, the energy-dependent term in eq. (3.2) provides a potentially large source of momentum mis-measurements in our analysis. This channel-dependent behavior can be seen in figure 13(a) for m_N =500 GeV. The increase in MET is found to be modest. In figure 13(b), we plot the combined MET differential distribution for representative m_N. To maximize the contributions to our signal rate, we impose the loose criterion

$$\not{p}_T < 50 \text{ GeV}. \tag{3.10}$$

The corresponding rate is given in the fourth row of table 5 and show that most events pass. Though technically difficult, tightening this cut can greatly enhance the signal-to-noise ratio.

To identify the heavy neutrino resonance in the complicated $\ell^\pm\ell^\pm+(n+2)j$ topology, we exploit that the $N \to \ell^\pm jj$ decay results in two very energetic jets that remain very central and possess a resonant invariant mass. In the $4j$ final-state channel, (rare) contributions from $N\ell^\pm W^\mp$ can lead to the existence of a second W boson in our signal. To avoid identifying a second W (or a continuum distribution) as the W boson from our heavy neutrino decay, we employ the following algorithm: (i) First consider all jets satisfying eq. (3.6) and require that at least one pair possesses an invariant mass close to M_W, i.e.,

$$|m_{j_m j_n} - M_W| < 20 \text{ GeV}. \tag{3.11}$$

(ii) If no such pair has an invariant mass within 20 GeV of M_W, then the event is rejected. (iii) If more than one pair satisfies eq. (3.11), including the situation where one jet can satisfy eq. (3.11) with multiple partners, we identify the jj-system with the highest p_T as the child W boson from the heavy neutrino decay. This last step is motived by the fact that the p_T of neutrino's decay products scale like $p_T \sim m_N/2$, and thus at larger values of m_N the W boson will become more boosted. This is contrary to $N\ell^\pm W^\mp$ and continuum events, in which all states are mostly produced close to threshold. In figure 14(a), we plot the reconstructed invariant mass of the dijet system satisfying this procedure and observe a very clear resonance at M_W. The corresponding rate is given in the fifth row of table 5 and show most events pass.

To remove background events from $t\bar{t}W$ production, events containing four or more jets with any three jets satisfying

$$|m_{jjj} - m_t| < 20 \text{ GeV} \tag{3.12}$$

are rejected. As this is a non-resonant distribution in the $N\ell + nj$ channels, its impact on the signal rate is minimal. The corresponding rate is given in the sixth row of table 5 and

JHEP02(2015)072

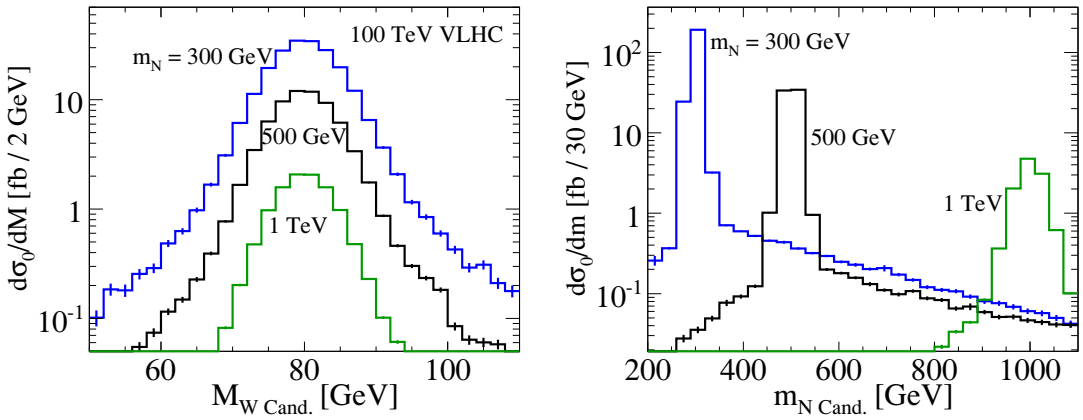

(a) (b)

Figure 14. Reconstructed invariant mass of the (a) W boson and (b) heavy N candidates for same m_N as figure 12.

m_N [GeV]	100	200	300	400	500	600
$\sigma_0^{\text{All Cuts}}$ [fb]	205	588	244	118	64.7	48.1
$\sigma_{\text{Tot}}^{\text{SM}}$ [ab]	16.3	115	53.2	22.2	11.4	6.01
$n_{2\sigma}^{b+\delta_{\text{Sys}}}(100\ \text{fb}^{-1})$	4	18	9	5	3	2
$n_{2\sigma}^{s}(100\ \text{fb}^{-1})$	8	16	11	9	7	6
m_N [GeV]	700	800	900	1000	1100	1200
$\sigma_0^{\text{All Cuts}}$ [fb]	23.4	14.4	10.5	7.79	4.61	4.01
$\sigma_{\text{Tot}}^{\text{SM}}$ [ab]	3.47	1.94	1.57	1.25	0.795	0.649
$n_{2\sigma}^{b+\delta_{\text{Sys}}}(100\ \text{fb}^{-1})$	2	1	1	1	1	1
$n_{2\sigma}^{s}(100\ \text{fb}^{-1})$	7	5	5	5	5	5

Table 6. Expected $\mu^{\pm}\mu^{\pm}jjX$ (bare) signal and SM background rates at 100 TeV VLHC after cuts. Number of background events and required signal events for 2σ sensitivity after 100 fb^{-1}.

show that nearly all events pass. A top quark-veto can be further optimized by introducing high-purity anti-b-tagging, e.g., ref. [89].

We identify N by imposing the m_N-dependent requirement on the two $(\ell_i, W_{\text{Cand.}})$ pairs and choose whichever system possesses an invariant mass closer to m_N. In figure 14(b), we plot the reconstructed invariant mass of this system observing very clear peaks at m_N. It is important to take into account that the width of the heavy neutrino grows like m_N^3, and reaches the 10 GeV-level at $m_N = 1$ TeV. Therefore, we apply the following width-sensitive cut:

$$|m_{N\ \text{Cand.}} - m_N| < \text{Max}(20\ \text{GeV},\ 3\Gamma_N). \tag{3.13}$$

The corresponding rate is given in the seventh row of table 5 and show most events pass.

JHEP02(2015)072

m_N [GeV]	100	200	300	400	500	600
$\sigma_0^{\text{All Cuts}}$ [fb]	408	1160	480	230	125	93.2
$\sigma_{\text{Tot}}^{\text{SM}}$ [ab]	196	4000	578	82.2	17.7	8.20
$n_{2\sigma}^{b+\delta_{\text{Sys}}}(100\ \text{fb}^{-1})$	27	434	71	13	4	3
$n_{2\sigma}^{s}(100\ \text{fb}^{-1})$	18	71	30	13	8	8
m_N [GeV]	700	800	900	1000	1100	1200
$\sigma_0^{\text{All Cuts}}$ [fb]	44.9	27.7	20.3	15.1	8.98	7.86
$\sigma_{\text{Tot}}^{\text{SM}}$ [ab]	4.79	2.68	2.07	1.87	1.29	0.932
$n_{2\sigma}^{b+\delta_{\text{Sys}}}(100\ \text{fb}^{-1})$	2	1	1	1	1	1
$n_{2\sigma}^{s}(100\ \text{fb}^{-1})$	6	5	5	5	5	5

Table 7. Same as table 6 for $e^{\pm}\mu^{\pm}jjX$.

The acceptance $\mathcal{A}$ of our signal rate, defined as

$$\mathcal{A} = \sigma_{\text{All Cuts}} \ / \ \sigma_{\text{Fidcuial Cuts+Kinematic Cuts+Smearing}}, \tag{3.14}$$

is given in the last row of table 5. The total bare rate for the $\mu\mu$ and μe channels at representative values of m_N are given, respectively, in the tables 6 and 7.

3.3 Background

Although there are no lepton-number violating processes in the SM, there exist rare processes with final-state, same-sign leptons as well as "faked" backgrounds from detector mismeasurement. Here we describe our estimate of the leading backgrounds to the final-state

$$pp \to \ell^{\pm}\ell'^{\pm} + n \geq 2j + X \tag{3.15}$$

for the $\mu\mu$ and $e\mu$ channels. The principle SM processes are $t\bar{t}X$, $W^{\pm}W^{\pm}X$, and electron charge misidentification. We model the parton-level matrix elements of these processes using MG5_aMC@NLO [78] and the CTEQ6L PDFs [73] with factorization and renormalization scales $Q = \sqrt{\hat{s}}/2$. We perform the background analysis in the same manner as for the signal-analysis.

3.3.1 $t\bar{t}$

At 100 TeV, radiative EW processes at $\alpha_s^2\alpha$ such as

$$p\ p\ \to\ t\ \bar{t}\ W^{\pm} \to\ b\ \bar{b}\ W^{+}\ W^{-}\ W^{\pm} \to\ \ell^{\pm}\ \ell'^{\pm}\ b\ \bar{b}\ j\ j\ \nu_{\ell}\ \nu_{\ell'}, \tag{3.16}$$

possess non-negligible cross sections. At LO, $\sigma(t\bar{t}W \to \mu^{\pm}\mu^{\pm}b\bar{b}jj\nu_{\mu}\nu_{\mu}) \approx 40\,\text{fb}$, and threatens discovery potential. At 14 TeV, $t\bar{t}W$ possesses a NLO K-factor of $K = 1.2$ [90]. As an estimate, this is applied at 100 TeV. As shown in table 8, the tight acceptance cuts reduce the rate by roughly 75%. Unlike the signal process, $t\bar{t}W$ produces two light neutrinos, an

JHEP02(2015)072

$\sigma(t\bar{t}W)$ [fb]	$e\mu$	$\mu\mu$
Fiducial + Kinematics + Smearing [$K = 1.2$] [Eq. (3.6)]	20.5	10.3 (26%)
Leading p_T Minimum [Eq. (3.7)]	16.5	8.23 (80%)
$\Delta R_{\ell j}$ Separation [Eq. (3.9)]	11.8	5.91 (72%)
$\not{E}_T$ Maximum [Eq. (3.10)]	3.58	1.78 (30%)
M_W Reconstruction [Eq. (3.11)]	2.54	1.27 (72%)
m_t Veto [Eq. (3.12)]	0.0452	0.0213 (2%)
$\sigma(t\bar{t})$ (Electron Charge Mis-ID) [fb]	$e\mu$	
Fiducial + Kinematics + Smearing [Eq. (3.6)] [$K = 0.96$]	94.5 $\times 10^3$ (21%)	
Leading p_T Minimum [Eq. (3.7)]	67.0 $\times 10^3$ (71%)	
$\Delta R_{\ell j}$ Separation [Eq. (3.9)]	55.2 $\times 10^3$ (82%)	
$\not{E}_T$ Maximum [Eq. (3.10)]	21.4 $\times 10^3$ (39%)	
M_W Reconstruction [Eq. (3.11)]	3.12 $\times 10^3$ (15%)	
m_t Veto [Eq. (3.12)]	3.12 $\times 10^3$ (100%)	
Charge Mis-ID [$\epsilon_{e\ \mathrm{Mis-ID}}$] [Eq. (3.20)]	10.9 (0.4%)	

Table 8. Acceptance rates for SM $t\bar{t}$ at 100 TeV pp collider.

inherent source of MET. After the MET cut, the background rate is reduced to the 2 fb level. Lastly, the decay chain

$$t \;\to\; b\,W \;\to\; b\,j\,j \tag{3.17}$$

can be reconstructed into a top quark. Rejecting any event with a three-jet invariant mass near the top quark mass, i.e., eq. (3.12), dramatically reduces this background to the tens of ab level. At this point, approximately 0.2% of events passing initial selection criteria survive.

At 100 TeV, the NLO $t\bar{t}$ cross section is estimated to be $\sigma(t\bar{t}) \approx 1.8\times 10^7$ fb [84]. Hence, rare top quark decays have the potential to spoil our sensitivity, e.g.,

$$pp \;\to\; t\,\bar{t} \;\to\; b\,\bar{b}\,W^+\,W^- \to\; b\,\bar{c}\,\ell^+\,\ell^{+\prime}\,\nu_\ell\,\nu_{\ell'}\,W^- + \text{c.c.}, \tag{3.18}$$

where a b-quark hadronizes into a B-meson that then decays semi-leptonically through the $b \to c\ell\nu_\ell$ subprocess, which is proportional to the small mixing $|V_{cb}|^2$. The MET and $\Delta R_{\ell j}$ cuts render the rate negligible [29]. Usage of high-purity anti-b tagging techniques [89] can further suppresses this process. The $b \to u$ transition offers a similar background but is $|V_{ub}/V_{cb}|^2 \sim (0.1)^2$ smaller [79].

3.3.2 Electron charge misidentification

An important source of background for the $e^\pm\mu^\pm$ channel is from electron charge misidentification in fully leptonic decays of top quark pairs:

$$p\,p \to t\,\bar{t} \to b\,\bar{b}\,W^+\,W^- \to b\,\bar{b}\,e^\pm\,\ell^\mp\,\nu_e\nu_\ell, \quad \ell = e,\ \mu. \tag{3.19}$$

JHEP02(2015)072

$\sigma(W^\pm W^\pm + 2j)$ [fb]	$e\mu$	$\mu\mu$
Fiducial + Kinematics + Smearing [Eq. (3.6)]	11.6	5.78 (11%)
Leading p_T Minimum [Eq. (3.7)]	9.45	4.72 (82%)
$\Delta R_{\ell j}$ Separation [Eq. (3.9)]	7.46	3.63 (77%)
$\not{E}_T$ Maximum [Eq. (3.10)]	2.56	1.28 (35%)
M_W Reconstruction [Eq. (3.11)]	0.132	0.0664 (5%)
m_t Veto [Eq. (3.12)]	0.132	0.0664 (100%)
$\sigma(W^\pm W^\pm W^\mp)$ [fb]	$e\mu$	$\mu\mu$
Fiducial + Kinematics + Smearing [$K = 1.8$] [Eq. (3.6)]	3.35	1.68 (13%)
Leading p_T Minimum [Eq. (3.7)]	2.53	1.26 (75%)
$\Delta R_{\ell j}$ Separation [Eq. (3.9)]	2.31	1.11 (87%)
$\not{E}_T$ Maximum [Eq. (3.10)]	0.754	0.375 (34%)
M_W Reconstruction [Eq. (3.11)]	0.735	0.368 (98%)
m_t Veto [Eq. (3.12)]	0.735	0.368 (100%)

Table 9. Acceptance rates for SM $W^\pm W^\pm$ at 100 TeV pp collider.

Such misidentification occurs when an electron undergoes bremsstrahlung in the tracker volume and the associated photon converts into an e^+e^- pair. If the electron of opposite charge carries a large fraction of the original electron's energy, then the oppositely charged electron may be misidentified as the primary electron. For muons, this effect is negligible due the near absence of photons converting to muons [91, 92]. At the CMS detector, the electron charge misidentification rate, $\epsilon_{\text{e Mis-ID}}$, has been determined as a function of generator-level η [92]. We assume a conservative, uniform rate of

$$\epsilon_{e\ \text{Mis-ID}} = 3.5 \times 10^{-3}. \tag{3.20}$$

To estimate the effect of electron charge mis-ID at 100 TeV, we consider eq. (3.19), normalized to NLO. Other charge mis-ID channels, including $Z + nj$, are coupling/phase space suppressed compared to $t\bar{t}$. The $t\bar{t}$ rate after selection cuts is recorded in table 8, and exists at the 100 pb level. We find that the electron charge mis-ID rate for eq. (3.19) can be as large as 11 fb before the $m_{N\ \text{Cand}}$ cut is applied. As either electron in the $e^\pm e^\pm$ channel can be tagged, the mis-ID background is the same size as the $e^\pm\mu^\pm$ channel. Applying the $m_{N\ \text{Cand}}$ cut we observe that the background quickly falls off for $m_N \gtrsim 200$ GeV. As with other backgrounds possessing final-state bottoms, high purity anti-b-tagging offers improvements. We conclude that the effects of charge misidentification are the dominant background in electron-based final states.

3.3.3 $W^\pm W^\pm$

The QCD and EW processes at orders $\alpha_s^2\alpha^2$ and α^3 , respectively,

$$p\,p \;\to\; W^\pm\,W^\pm\,j\,j \tag{3.21}$$
$$p\,p \;\to\; W^\pm\,W^\pm\,W^\mp \tag{3.22}$$

JHEP02(2015)072

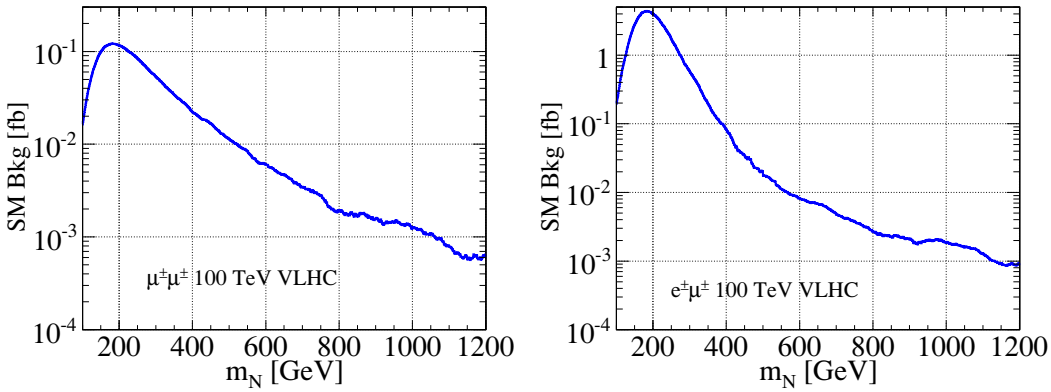

(a) (b)

Figure 15. Total SM background versus m_N for (a) $\mu^{\pm}\mu^{\pm}$ and (b) $e^{\pm}\mu^{\pm}$ channels at 100 TeV.

present a challenging background due to their sizable rates and kinematic similarity to the signal process. The triboson production rate at NLO in QCD for 14 TeV LHC has been calculated [93]. As an estimate, we apply the 14 TeV K-factor of $K = 1.8$ to the 100 TeV LO $W^{\pm}W^{\pm}W^{\mp}$ channel. After requiring the signal definition criteria, we find the $W^{\pm}W^{\pm}$ backgrounds are present at the several fb-level. Like $t\bar{t}$, the $W^{\pm}W^{\pm}X$ final states possess light neutrinos and non-negligible MET. Imposing a maximum on the allowed MET further reduces the background by about 35%. As no $W \to jj$ decay exists in the QCD process, the reconstructed M_W requirement drops the rate considerably. After the m_t veto, the SM $W^{\pm}W^{\pm}X$ rate is 0.4 (0.9) fb for the $\mu\mu$ ($e\mu$) channel.

For all background channels, we apply the m_N-dependent cut given in eq. (3.13) on the invariant mass of the reconstructed W candidate with either charged lepton. The total expected SM background after all selection cuts as a function of m_N are given for the $\mu\mu$ channel in figure 15(a), and the $e\mu$ channel in figure 15(b). The total expected SM background for representative values of m_N are given in tables 6 and 7, respectively. For these channels, we find a SM background of $1 - 115$ ab and $1 - 4000$ ab for the neutrino masses considered. For both channels, the background is greatest for $m_N \lesssim 400$ GeV and become comparable for $m_N \gtrsim 600$ GeV.

3.4 Discovery potential at 100 TeV

We now estimate the discovery potential at the 100 TeV VLHC of L-violation via same-sign leptons and jets. We quantify this using Poisson statistics. Details of our treatment can be found in appendix C. The total neutrino cross section is related to the total bare cross section by the expression

$$\sigma(\ell^{\pm}\ell'^{\pm}jj + X) = S_{\ell\ell'} \times \sigma_0(\ell^{\pm}\ell'^{\pm}jj + X). \tag{3.23}$$

We consider two scenarios for $S_{\mu\mu}$, one used by ref. [29], dubbed the "optimistic" scenario,

$$S_{\mu\mu} = 6 \times 10^{-3}, \tag{3.24}$$

JHEP02(2015)072

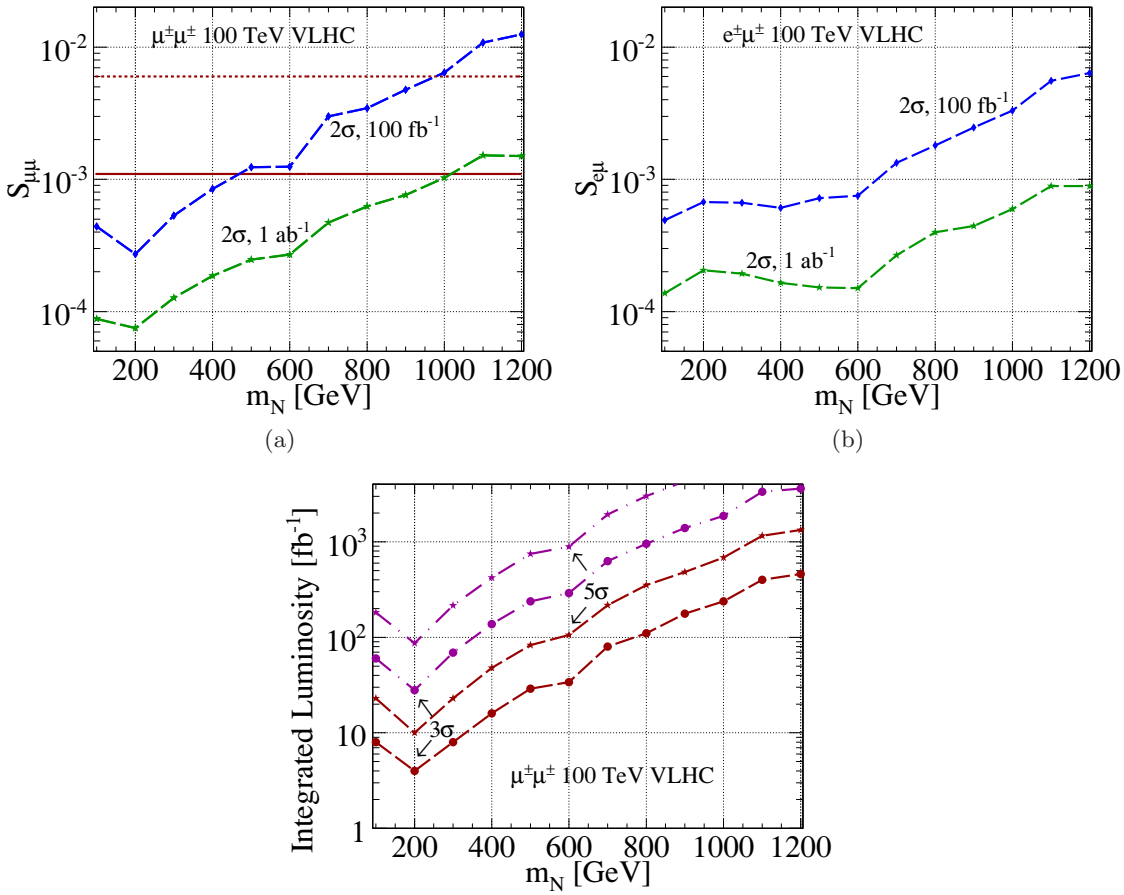

Figure 16. At 100 TeV and as a function of m_N, the 2σ sensitivity to $S_{\ell\ell'}$ after 100 fb^{-1} (dash-diamond) and 1 ab^{-1} (dash-star) for the (a) $\mu^\pm\mu^\pm$ and (b) $e^\pm\mu^\pm$ channels. The optimistic (pessimistic) bound is given by the solid (short-dash) horizontal line. (c) The required luminosity for a 3 (dash-circle) and 5σ (dash-star) discovery in the $\mu^\pm\mu^\pm$ channel.

and the more stringent value obtained in eq. (2.17), dubbed the "pessimistic" scenario,

$$S_{\mu\mu} = 1.1 \times 10^{-3}. \tag{3.25}$$

For $S_{e\mu}$, we use the m_N-dependent quantity obtained in eq. (2.16), i.e., $10^{-5} - 10^{-6}$. We introduce a 20% systematic uncertainty by making the following scaling to the SM background cross section

$$\sigma_{\rm SM} \to \delta_{\rm Sys} \times \sigma_{\rm SM}, \quad \delta_{\rm Sys} = 1.2. \tag{3.26}$$

For the $\mu\mu$ and $e\mu$ channels, respectively, the maximum number of background events and requisite number of signal events at a 2σ significance after 100 fb^{-1} are given in tables 6 and 7. For the $\mu\mu$ channel, these span $1-18$ background and $5-16$ signal events; for $e\mu$, $1-434$ and $5-71$ events.

We translate this into sensitivity to the mixing parameter $S_{\ell\ell'}$ and plot the 2σ contours in $S_{\ell\ell'} - m_N$ space assuming 100 fb^{-1} (dash-diamond) and 1 ab^{-1} (dash-star) for the $\mu\mu$

JHEP02(2015)072

	$\mathcal{L}$	$S_{e\mu}$(100 TeV)	$S_{\mu\mu}$(100 TeV)	$S_{\mu\mu}$(14 TeV)
2σ	$100\,\text{fb}^{-1}$	4.9×10^{-4}	2.7×10^{-4}	1.4×10^{-4}
	$1\ \text{ab}^{-1}$	1.4×10^{-4}	7.5×10^{-5}	3.1×10^{-5}
375 GeV	$100\,\text{fb}^{-1}$	6×10^{-4}	7.5×10^{-4}	3×10^{-3}
	$1\ \text{ab}^{-1}$	1.7×10^{-4}	1.8×10^{-4}	5.5×10^{-4}
500 GeV	$100\,\text{fb}^{-1}$	7.2×10^{-4}	1.2×10^{-3}	8×10^{-3}
	$1\ \text{ab}^{-1}$	1.5×10^{-4}	2.5×10^{-4}	1.1×10^{-3}

Table 10. Sensitivity to the mixing parameter $S_{\ell\ell'}$ at the 14 TeV LHC and 100 TeV VLHC.

100 TeV	$2\sigma(100\,\text{fb}^{-1})$	$5\sigma(100\,\text{fb}^{-1})$	$5\sigma(1\ \text{ab}^{-1})$	$\mathcal{L}_{5\sigma}$(375 GeV)	$\mathcal{L}_{5\sigma}$(500 GeV)
Optimistic	980 GeV	580 GeV	1070 GeV	$40\,\text{fb}^{-1}$	$80\,\text{fb}^{-1}$
Pessimistic	470 GeV	215 GeV	615 GeV	$380\,\text{fb}^{-1}$	$750\,\text{fb}^{-1}$
14 TeV	$2\sigma(100\,\text{fb}^{-1})$	$5\sigma(100\,\text{fb}^{-1})$	$5\sigma(1\ \text{ab}^{-1})$	$\mathcal{L}_{5\sigma}$(375 GeV)	$\mathcal{L}_{5\sigma}$(500 GeV)
Optimistic	465 GeV	270 GeV	530 GeV	$300\,\text{fb}^{-1}$	$810\,\text{fb}^{-1}$
Pessimistic	255 GeV	135 GeV	280 GeV	$2.6\ \text{ab}^{-1}$	$6.9\ \text{ab}^{-1}$

Table 11. Sensitivity to heavy neutrino production in the $\mu\mu$ channel at 14 and 100 TeV.

[figure 16(a)] and $e\mu$ [figure 16(b)] channels. In the $\mu\mu$ scenario and $m_N = 500$ GeV, a mixing at the level of $S_{\mu\mu} = 1.2 \times 10^{-3}$ (2.5×10^{-4}) with 100^{-1} ($1\ \text{ab}^{-1}$) can be probed. The optimistic (pessimistic) bound is given by the solid (short-dash) horizontal line. In the $e\mu$ scenario and the same mass, we find sensitivity to $S_{e\mu} = 7.2$ (1.5) $\times 10^{-4}$. For the $e\mu$ channel, the EW+$0\nu\beta\beta$ bound is at the $10^{-6} - 10^{-5}$ level. Sensitivity to $S_{\ell\ell'}$ at 100 TeV is summarized in table 10.

Comparatively, we observe a slight "dip" (broad "bump") in the $\mu\mu$ ($e\mu$) curve around 200 GeV. For the $\mu\mu$ channel, this is due to the low signal acceptance rates for Majorana neutrinos very close to the W threshold; the search methodology for m_N near or below the M_W has been studied elsewhere [27, 29]. For $m_N \geq 200$ GeV, the signal acceptance rate grows rapidly, greatly increasing sensitivity. In the $e\mu$ channel, the electron charge mis-ID background is greatest in the region around 200 GeV and quickly dwindles for larger m_N. In the low-mass regime, we find greater sensitivity in the $\mu\mu$ channel. However, due to flavor multiplicity and comparable background rates, the $e\mu$ channel has greater sensitivity in the large-m_N regime.

In figure 16(c), we plot as a function of m_N the required luminosity for a 3σ (circle) and 5σ (star) discovery in the $\mu\mu$ channel for the pessimisticc (purple, dash-dot) and optimistic (red, dash) mixing scenarios. With $100\,\text{fb}^{-1}(1\ \text{ab}^{-1})$ and in the optimistic scenario, a Majorana neutrino with $m_N = 580$ (1070) GeV can be discovered at 5σ significance; with the same integrated luminosity but in the pessimistic scenario, the reach is $m_N = 215$ (615) GeV. In the optimistic (pessimistic) scenario, for a 375 GeV Majorana neutrino, a benchmark used by ref. [29], a 5σ discovery can be achieved with 40 (350) fb^{-1}; for 500 GeV, this is 80 (750) fb^{-1}. Sensitivity to m_N at 100 TeV is summarized in table 11.

JHEP02(2015)072

Lepton Cuts	Jet Cuts	Other Cuts
$\Delta R_{\ell\ell} > 0.2$ p_T^ℓ ($p_T^{\ell\,\mathrm{Max}}$) > 10 (30) GeV $\lvert\eta^\ell\rvert < 2.4$	$\Delta R_{jj} > 0.4$ p_T^j ($p_T^{j\,\mathrm{Max}}$) > 15 (40) GeV $\lvert\eta^j\rvert < 2.4$ $\lvert M_W^{\mathrm{Candidate}} - M_W\rvert < 20$ GeV $\lvert m_{jjj} - m_t\rvert < 20$ GeV (Veto)	$\Delta R_{\ell j}^{\mathrm{Min}} > 0.5$ $\not{E}_T < 35$ GeV $\lvert m_N^{\mathrm{Candidate}} - m_N\rvert < 20$ GeV

Table 12. Parton-level cuts on 14 TeV $\mu^\pm\mu^\pm jjX$ Analysis.

$\sigma \setminus m_N$ [GeV]	100	200	300	400	500	600	700
$\sigma_0^{\mathrm{All\ Cuts}}$ [fb]	576	132	36.0	14.0	6.28	3.05	1.55
$\sigma_{\mathrm{Tot}}^{\mathrm{SM}}$ [ab]	14.1	18.6	5.62	2.05	0.837	0.393	0.195
$n_{2\sigma}^{b+\delta_{\mathrm{Sys}}}(100\ \mathrm{fb}^{-1})$	4	4	2	1	1	0	0
$n_{2\sigma}^{s}(100\ \mathrm{fb}^{-1})$	8	8	6	5	5	4	4

Table 13. Same as table 6 for 14 TeV LHC.

3.5 Updated discovery potential at 14 TeV LHC

We update the 14 TeV LHC discovery potential to heavy Majorana neutrinos above the W boson threshold decaying to same-sign muons. Our procedure largely follows the 100 TeV scenario but numerical values are based on ref. [29]. Signal-wise, we require exactly two same-sign muons (vetoing additional leptons) and at least two jets (allowing additional jets) satisfying the cuts listed in table 12. Differences from the analysis introduced by ref. [29] include: updated smearing parameterization given in eqs. (3.2) and (3.3); an $\not{E}_T$ requirement based on the ATLAS detector capabilities given in ref. [40]; cuts on the leading charged lepton and jet; and more stringent requirements on the W and N candidate masses. These differences sacrifice sensitivity to $m_N \lesssim 100$ GeV for high-mass reach. For our NNLO in QCD K-factor, we use $K = 1.2$, as given in eq. (2.20). We report the bare heavy neutrino rate after all cuts for representative m_N in the first row of table 13. The total bare rate ranges from $2 - 580$ fb for $m_N = 100 - 700$ GeV.

As previously discussed or shown, the $t\bar{t}$ background for the dimuon channel is negligible, so we focus on $W^\pm W^\pm$ pairs. For triboson production, an NLO in QCD K factor of $K = 1.8$ is applied [93]. After all cuts, the expected SM background for representative m_N is given in the second row table 13. After the m_N-dependent cut, the expected SM background rate reaches at most 19 ab. Like the 100 TeV case, a 20% systematic is introduced into the background. For the $\mu\mu$ and $e\mu$ channels, respectively, The maximum number of background events and requisite number of signal events at a 2σ significance after 100 fb^{-1} are given in the third and fourth rows, respectively, of table 13.

In figure 17(a), we plot the 2σ sensitivity to the mixing coefficient $S_{\mu\mu}$ after 100 fb^{-1} (dash-diamond) and 1 ab^{-1} (dash-star). For the benchmark $m_N = 375$ GeV, a mixing at the level of $S_{\mu\mu} = 3 \times 10^{-3}$ (5.5×10^{-4}) with 100^{-1} (1 ab^{-1}) can be probed; for

JHEP02(2015)072

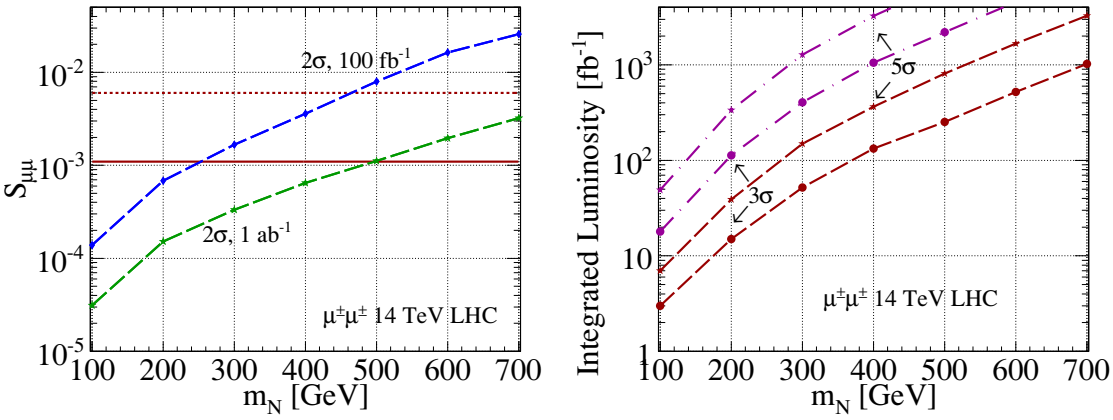

(a) (b)

Figure 17. At 14 TeV, (a) same as figure 16(a); (b) same as figure 16(c).

$m_N = 500$ GeV, we find sensitivity to be $S_{\mu\mu} = 8 \times 10^{-3}$ (1.1×10^{-4}). The optimistic (pessimistic) bound is given by the solid (short-dash) horizontal line. Sensitivity to $S_{\mu\mu}$ at 14 TeV is summarized in table 10.

In figure 17(b), we plot as a function of m_N the required luminosity for a 3σ (circle) and 5σ (star) discovery in the $\mu\mu$ channel for the pessimistic (purple, dash-dot) and optimistic (red, dash) mixing scenarios. With 100 fb^{-1} (1 ab^{-1}) and in the optimistic scenario, a Majorana neutrino with $m_N = 270$ (530) GeV can be discovered at 5σ significance; in the pessimistic scenario, the reach is $m_N = 135$ (280) GeV. In the optimistic (pessimistic) scenario, for the 375 GeV benchmark, a 5σ discovery can be achieved with 300 (2600) fb^{-1}; for 500 GeV, this is 810 (6900) fb^{-1}. Sensitivity to m_N at 14 TeV is summarized in table 11.

4 Summary

The search for a heavy Majorana neutrino at the LHC is of fundamental importance. It is complimentary to the neutrino oscillation programs and, in particular, neutrinoless double-beta decay experiments. We have studied the production of a heavy Majorana neutrino at hadron colliders and its lepton-number violating decay as in eq. (3.1), including the NNLO DY contribution, the elastic and inelastic $p\gamma \to N\ell j$ processes, and the DIS $pp \to N\ell jj$ process via $W\gamma^*$ fusion. We have determined the discovery potential of the same-sign dilepton signal at a future 100 TeV pp collider, and updated the results at the 14 TeV LHC. We summarize our findings as follows:

- Vector boson fusion processes,e.g., $W\gamma \to N\ell$, become increasingly more important at higher collider energies and larger mass scales due to collinear logarithmic enhancements of the cross section. At the 14 TeV LHC, the three contributing channels of elastic, inelastic and DIS are comparable in magnitude, while at the 100 TeV VLHC, the tendency, in descending importance, is DIS, inelastic, and elastic; see figures 4(a) and 4(b).

JHEP02(2015)072

- We approximately computed the QCD corrections up to NNLO of the DY production of $N\ell$ to obtain the K-factor. We found it to span $1.2 - 1.5$ for m_N values between 100 GeV and 1 TeV at 14 and 100 TeV pp collisions, and is summarized in table 1.

- The $W\gamma$ fusion processes surpasses the DY mechanism at $m_N \sim 1$ TeV (770 GeV) at the 14 TeV LHC (100 TeV VLHC); see figure 4(c) [4(d)]. However, we disagree with the results of refs. [36], where higher order contributions dominating over the LO DY production at $m_N \geq 200$ GeV were claimed. The discrepancy is attributed to their too low a p_T^j cut that overestimates the contribution of initial-state radiation based on a tree-level calculation.

- We have introduced a systematic treatment for combining initial-state photons from various channels and predict cross sections that are rather stable against the scale choices, typically less than 20%. The exception is the inelastic process, which is rather sensitive to the scale $\Lambda_\gamma^{\rm El}$ where the elastic and inelastic processes are separated. Variation of this scale could lead to about a 30% uncertainty. Scale dependence is shown in figure 10 and the results summarized in table 3.

- We quantified the signal observability by examining the SM backgrounds. We conclude that, with the currently allowed mixing $|V_{\mu N}|^2 < 6 \times 10^{-3}$, a 5σ discovery can be made via the same-sign dimuon channel for $m_N = 530$ (1070) GeV at the 14 TeV LHC (100 TeV VLHC) after 1 ab^{-1}; see table 11. Reversely, for $m_N = 500$ GeV and the same integrated luminosity, a mixing $|V_{\mu N}|^2$ of the order 1.1×10^{-3} (2.5×10^{-4}) may be probed; see table 10. This study represents the first investigation into heavy Majorana neutrino production in 100 TeV pp collisions.

Acknowledgments

We would like to thank Darin Baumgartel, Ayres Freitas, Jose Kenichi, Olivier Mattelaer, Jim Mueller, Juan Rojo, Josh Sayre, and Brock Tweedie for valuable discussions. D.A. acknowledges the Brazilian agency FAPESP for the support and PITT-PACC for its generous hospitality while doing part of this research. The work of T.H. was supported in part by the U.S. Department of Energy under Grant No. DE-FG02-95ER40896 and in part by the PITT-PACC. R.R. acknowledges support from the University of Pittsburgh and the generosity of the Institute for High Energy Physics Center for Future High Energy Physics and the Korea Institute for Advance Science.

A Elastic photon PDF

The elastic photon PDF for a proton is given analytically by [49]

$$f_{\gamma/p}^{\rm El}(\xi) = \frac{\alpha_{\rm EM}}{\pi}\frac{(1-\xi)}{\xi}\left[\varphi\left(\frac{\Lambda_\gamma^{\rm El\,2}}{Q_0^2}\right) - \varphi\left(\frac{Q_{\rm min}^2}{Q_0^2}\right)\right], \qquad \alpha_{\rm EM} \approx 1/137, \tag{A.1}$$

$$Q_{\rm min}^2 = m_p^2 y, \qquad y = \frac{\xi^2}{(1-\xi)}, \qquad Q_0^2 = 0.71\ {\rm GeV}^2, \qquad m_p = 0.938\ {\rm GeV}, \tag{A.2}$$

JHEP02(2015)072

$$\varphi(x) = (1+ay)\left[-\log\left(1+\frac{1}{x}\right)+\sum_{k=1}^{3}\frac{1}{k(1+x)^k}\right]+\frac{y(1-b)}{4x(1+x)^3}$$
$$+c\left(1+\frac{y}{4}\right)\left[\log\left(\frac{1+x-b}{1+x}\right)+\sum_{k=1}^{3}\frac{b^k}{k(1+x)^k}\right], \tag{A.3}$$
$$a = \frac{1}{4}(1+\mu_p^2)+\frac{4m_p^2}{Q_0^2}\approx 7.16, \quad b = 1-\frac{4m_p^2}{Q_0^2}\approx -3.96, \quad c=\frac{\mu_p^2-1}{b^4}\approx 0.028. \tag{A.4}$$

Here, $\Lambda_\gamma^{\rm El}$ is a upper limit on elastic momentum transfers such that $f_{\gamma/p}^{\rm El}=0$ for $Q_\gamma > \Lambda_\gamma^{\rm El}$. In eq. (A.1), and later in eq. (B.2), since $Q_\gamma \ll m_Z$, $\alpha(\mu=Q_\gamma)\approx\alpha_{\rm EM}\approx 1/137$ is used. In the hard scattering matrix elements, $\alpha(\mu=M_Z)$ is used. See ref. [57] for further details.

Equation (A.1) has been found to agree well with data from TeV-scale collisions at $Q_\gamma \sim m_\mu$ [67]. However, applications to cases with larger momentum transfers and finite angles lead to large errors and increase scale sensitivity. Too large a choice for $\Lambda_\gamma^{\rm El}$ will lead to overestimate of cross sections [49]. However, we observe negligible growth in $f_\gamma^{\rm El}$ at scales well above $\Lambda_\gamma^{\rm El}=1-2$ GeV, in agreement with ref. [62].

Briefly, we draw attention to a typo in the original manuscript that derives eq. (A.1). This has been only scantly been mentioned in past literature [54, 61]. The sign preceding the "$y(1-b)$" term of φ in eq. (A.3) is erroneously flipped in eq. (D7) of ref. [49]. Both CalcHEP [94] and MG5_aMC@NLO [78] have the correct sign in their default PDF libraries.

At these scales, the gauge state γ is a understood to be a linear combination of discrete states: the physical (massless) photon and (massive) vector mesons $(\omega,\phi,\ldots)$, and a continuous mass spectrum, a phenomenon known as generalized vector meson dominance (GVMD) [95]. An analysis of ZEUS measurements of the F_2 structure function at $Q_\gamma^2 < m_p^2$ and Bjorken-$x \ll 1$ concludes that GMVD effects are included in the usual dipole parameterizations of the proton's electric and magnetic form factors $G_{\rm E}$ and $G_{\rm M}$ [85]. Thus, the radiation of vector mesons by a proton that are then observed as photon has been folded into eq. (A.1).

B Inelastic photon PDF

Following the methodology of ref. [57], the inelastic $N\ell X$ cross section is given explicitly by

$$\sigma_{\rm Inel}(pp\to N\ell^\pm X+\text{anything})$$
$$=\sum_{q,q'}\int_{\tau_0}^1 d\xi_1\int_{\tau_0/\xi_1}^1 d\xi_2\int_{\tau_0/\xi_1/\xi_2}^1 dz$$
$$\times\left[f_{q/p}\left(\xi_1,Q_f^2\right)\ f_{\gamma/q'}\left(z,Q_\gamma^2\right)\ f_{q'/p}\left(\xi_2,Q_f^2\right)\hat{\sigma}\left(q_1\gamma_2\right)+(1\leftrightarrow 2)\right], \tag{B.1}$$
$$\tau_0 = m_N^2/s, \quad \tau=\hat{s}/s=\xi_1\xi_2 z.$$

The Weizsäcker-Williams photon structure function [86, 87] is given by

$$f_{\gamma/q}(z,Q_\gamma^2)=\frac{\alpha_{\rm EM}\ e_q^2}{2\pi}\left(\frac{1+(1-z)^2}{z}\right)\log\left(\frac{Q_\gamma^2}{\Lambda_\gamma^{\rm Inel}}\right), \quad \alpha_{\rm EM}\approx 1/137, \tag{B.2}$$

JHEP02(2015)072

where $e_q^2 = 4/9$ $(1/9)$ for up-(down-)type quarks and $\Lambda_\gamma^{\rm Inel}$ is a low-momentum transfer cutoff. In DGLAP-evolved photon PDFs [72], $\Lambda_\gamma^{\rm Inel}$ is taken as the mass of the participating quark. Ref. [57] argues a low-energy cutoff $\mathcal{O}(1-2)\,\text{GeV}$ so that the associated photon is sufficiently off-shell for the parton model to be valid. As demonstrated, taking $\Lambda_\gamma^{\rm Inel} = \Lambda_\gamma^{\rm El} = \mathcal{O}(1-2)$ GeV allows for the inclusion of non-perturbative phenomena without worry of double counting of phase space.

Fixing z and defining $\xi_\gamma \equiv \xi_2 z$, we have the relationships

$$\tau_0 = \min\left(\xi_1\xi_2 z\right) = \min\left(\xi_1\xi_\gamma\right) \implies \min(\xi_\gamma) = \frac{\tau_0}{\xi_1} \text{ for fixed } \xi_1. \tag{B.3}$$

Physically, ξ_γ is the fraction of proton energy carried by the initial-state photon. Eq. (B.2) can be expressed into the more familiar two-PDF factorization theorem, i.e., eq. (2.3), by grouping together the convolutions about $f_{q'/p}$ and $f_{\gamma/q'}$:

$$\begin{aligned}
&\sum_{q'}\int_{\tau_0/\xi_1}^1 d\xi_2 \int_{\tau_0/\xi_1/\xi_2}^1 dz\ f_{\gamma/q'}(z)\ f_{q'/p}(\xi_2) \\
&\qquad = \sum_{q'}\int_{\tau_0/\xi_1}^1 \frac{d\xi_\gamma}{z}\int_{z_{\min}}^1 dz\ f_{\gamma/q'}(z)\ f_{q'/p}\left(\frac{\xi_\gamma}{z}\right) &\text{(B.4)}\\
&\qquad = \int_{\tau_0/\xi_1}^1 d\xi_\gamma\ f_{\gamma/p}^{\rm Inel}(\xi_\gamma) &\text{(B.5)}\\
f_{\gamma/p}^{\rm Inel}\left(\xi_\gamma, Q_\gamma^2, Q_f^2\right) &\equiv \sum_{q'}\int_{z_{\min}=\xi_\gamma}^1 \frac{dz}{z}\ f_{\gamma/q'}\left(z, Q_\gamma^2\right)\ f_{q'/p}\left(\frac{\xi_\gamma}{z}, Q_f^2\right). &\text{(B.6)}
\end{aligned}$$

The minimal fraction z of energy that can be carried away by the photon from the quark corresponds to when the quark has the maximum fraction ξ_2 of energy from its parent proton. Thus, for a fixed ξ_γ, we have

$$1 = \max(\xi_2) = \max\left(\frac{\xi_\gamma}{z}\right) = \frac{\xi_\gamma}{\min(z)} \implies \min(z) = \xi_\gamma. \tag{B.7}$$

The resulting expression is

$$\begin{aligned}
&\sigma_{\rm Inel}(pp \to N\ell^\pm X) \\
&\quad = \sum_q \int_{\tau_0}^1 d\xi_1 \int_{\tau_0/\xi_1}^1 d\xi_2 \left[\ f_{q/p}\left(\xi_1, Q_f^2\right)\ f_{\gamma/p}^{\rm Inel}\left(\xi_2, Q_\gamma^2, Q_f^2\right)\hat{\sigma}\left(q_1\gamma_2\right) + (1 \leftrightarrow 2)\right] &\text{(B.8)}
\end{aligned}$$

Real, initial-state photons from inelastic quark emissions can be studied in MG5 by linking the appropriate Les Houches accord PDFs (LHAPDF) libraries [96] and using the MRST2004QED [72] or NNPDF QED [97] PDF sets. With this prescription, sub-leading (but important) photon substructure effects [56], e.g., $P_{g\gamma}$ splitting functions, are included in evolution equations.

JHEP02(2015)072

C Poisson statistics

To determine the discovery potential at a particular significance, we first translate significance into a corresponding confidence level (CL),[6] e.g.,

$$2\sigma \leftrightarrow 95.45\%\ \text{CL}, \quad 3\sigma \leftrightarrow 99.73\%\ \text{CL}, \quad 5\sigma \leftrightarrow 99.9999\%\ \text{CL}. \tag{C.1}$$

Given an given integrated luminosity $\mathcal{L}$, SM background rate $\sigma_{\rm SM}$, and CL, say 95.45% CL, we solve for the maximum number of background-only events, denoted by n^b, using the Poisson distribution:

$$0.9545 = \sum_{k=0}^{n^b} P\left(k|\mu^b = \sigma_{\rm SM}\mathcal{L}\right) = \sum_{k=0}^{n^b} \frac{(\sigma_{\rm SM}\mathcal{L})^k}{k!} e^{-\sigma_{\rm SM}\mathcal{L}}. \tag{C.2}$$

The requisite number of signal events at a 95.45% CL (or 2σ significance) is obtained by solving for the mean number of signal events μ^s such that a mean number of total expected events $(\mu^s + \mu^b)$ will generate n^b events only $4.55\%(= 100\% - 95.45\%)$ of the time, i.e., find μ^s such that

$$P\left(k = n^b|\mu = \mu^s + \mu^b\right) = \frac{(\mu^s + \mu^b)^{n^b}}{(n^b)!} e^{-(\mu^s+\mu^b)} = 0.0455. \tag{C.3}$$

The 2σ sensitivity to nonzero $S_{\ell\ell}$ is then

$$S^{2\sigma}_{\ell\ell'} = \frac{\mu^s}{\mathcal{L} \times \sigma_{\text{Tot }0}}. \tag{C.4}$$

For fixed signal σ_s and background $\sigma_{\rm SM}$ rates, $\mu^s + \mu^b = (\sigma_s + \sigma_{\rm SM}) \times \mathcal{L}$. The required luminosity for a 2σ discovery can then be obtained by solving eq. (C.3) for $\mathcal{L}$.

References

[1] R.N. Mohapatra and P.B. Pal, *Massive neutrinos in physics and astrophysics. Second edition*, *World Sci. Lect. Notes Phys.* **60** (1998) 1 [*World Sci. Lect. Notes Phys.* **72** (2004) 1] [INSPIRE].

[2] J. Gluza, *On teraelectronvolt Majorana neutrinos*, *Acta Phys. Polon.* **B 33** (2002) 1735 [hep-ph/0201002] [INSPIRE].

[3] M. Fukugita and T. Yanagida, *Physics of neutrinos and applications to astrophysics*, Springer, Berlin Germany (2003).

[4] V. Barger, D. Marfatia and K. Whisnant, *Progress in the physics of massive neutrinos*, *Int. J. Mod. Phys.* **E 12** (2003) 569 [hep-ph/0308123] [INSPIRE].

[6] We use σ-sensitivity and CL interchangeably in the text.

JHEP02(2015)072

[5] Particle Data Group collaboration, S. Eidelman et al., *Review of particle physics*, *Phys. Lett.* **B 592** (2004) 1 [INSPIRE].

[6] R.N. Mohapatra and A.Y. Smirnov, *Neutrino mass and new physics*, *Ann. Rev. Nucl. Part. Sci.* **56** (2006) 569 [hep-ph/0603118] [INSPIRE].

[7] A. Strumia and F. Vissani, *Neutrino masses and mixings and...*, hep-ph/0606054 [INSPIRE].

[8] M.C. Gonzalez-Garcia and M. Maltoni, *Phenomenology with massive neutrinos*, *Phys. Rept.* **460** (2008) 1 [arXiv:0704.1800] [INSPIRE].

[9] P. Minkowski, $\mu \to e\gamma$ *at a rate of one out of 1-billion muon decays?*, *Phys. Lett.* **B 67** (1977) 421 [INSPIRE].

[10] T. Yanagida, *Horizontal symmetry and masses of neutrinos*, *Conf. Proc.* **C 7902131** (1979) 95 [INSPIRE].

[11] P. Van Nieuwenhuizen and D.Z. Freedman, *Supergravity. Proceedings, workshop at stony brook, 27–29 September 1979*, North-Holland, Amsterdam, Netherlands (1979).

[12] P. Ramond, *The family group in grand unified theories*, hep-ph/9809459 [INSPIRE].

[13] S.L. Glashow, *The future of elementary particle physics*, *NATO Sci. Ser.* **B 59** (1980) 687.

[14] R.N. Mohapatra and G. Senjanović, *Neutrino mass and spontaneous parity violation*, *Phys. Rev. Lett.* **44** (1980) 912 [INSPIRE].

[15] M. Gell-Mann, P. Ramond and R. Slansky, *Complex spinors and unified theories*, *Conf. Proc.* **C 790927** (1979) 315 [arXiv:1306.4669] [INSPIRE].

[16] J. Schechter and J.W.F. Valle, *Neutrino masses in* $\mathrm{SU}(2) \times \mathrm{U}(1)$ *theories*, *Phys. Rev.* **D 22** (1980) 2227 [INSPIRE].

[17] R.E. Shrock, *General theory of weak leptonic and semileptonic decays. 1. Leptonic pseudoscalar meson decays, with associated tests for and bounds on, neutrino masses and lepton mixing*, *Phys. Rev.* **D 24** (1981) 1232 [INSPIRE].

[18] J. Schechter and J.W.F. Valle, *Neutrino decay and spontaneous violation of lepton number*, *Phys. Rev.* **D 25** (1982) 774 [INSPIRE].

[19] N. Arkani-Hamed, L.J. Hall, H. Murayama, D. Tucker-Smith and N. Weiner, *Small neutrino masses from supersymmetry breaking*, *Phys. Rev.* **D 64** (2001) 115011 [hep-ph/0006312] [INSPIRE].

[20] F. Borzumati and Y. Nomura, *Low scale seesaw mechanisms for light neutrinos*, *Phys. Rev.* **D 64** (2001) 053005 [hep-ph/0007018] [INSPIRE].

[21] A. de Gouvêa, *See-saw energy scale and the LSND anomaly*, *Phys. Rev.* **D 72** (2005) 033005 [hep-ph/0501039] [INSPIRE].

[22] A. de Gouvêa, J. Jenkins and N. Vasudevan, *Neutrino phenomenology of very low-energy seesaws*, *Phys. Rev.* **D 75** (2007) 013003 [hep-ph/0608147] [INSPIRE].

[23] W.-Y. Keung and G. Senjanović, *Majorana neutrinos and the production of the right-handed charged gauge boson*, *Phys. Rev. Lett.* **50** (1983) 1427 [INSPIRE].

[24] D.A. Dicus, D.D. Karatas and P. Roy, *Lepton nonconservation at supercollider energies*, *Phys. Rev.* **D 44** (1991) 2033 [INSPIRE].

[25] A. Pilaftsis, *Radiatively induced neutrino masses and large Higgs neutrino couplings in the standard model with Majorana fields*, *Z. Phys.* **C 55** (1992) 275 [hep-ph/9901206] [INSPIRE].

JHEP02(2015)072

[26] A. Datta, M. Guchait and A. Pilaftsis, *Probing lepton number violation via Majorana neutrinos at hadron supercolliders*, *Phys. Rev.* **D 50** (1994) 3195 [hep-ph/9311257] [INSPIRE].

[27] T. Han and B. Zhang, *Signatures for Majorana neutrinos at hadron colliders*, *Phys. Rev. Lett.* **97** (2006) 171804 [hep-ph/0604064] [INSPIRE].

[28] F. del Aguila, J.A. Aguilar-Saavedra and R. Pittau, *Heavy neutrino signals at large hadron colliders*, *JHEP* **10** (2007) 047 [hep-ph/0703261] [INSPIRE].

[29] A. Atre, T. Han, S. Pascoli and B. Zhang, *The search for heavy Majorana neutrinos*, *JHEP* **05** (2009) 030 [arXiv:0901.3589] [INSPIRE].

[30] W. Chao, Z.G. Si, Y.J. Zheng and S. Zhou, *Testing the realistic seesaw model with two heavy majorana neutrinos at the CERN Large Hadron Collider*, *Phys. Lett.* **B 683** (2010) 26 [arXiv:0907.0935] [INSPIRE].

[31] J.A. Aguilar-Saavedra, F. Deppisch, O. Kittel and J.W.F. Valle, *Flavour in heavy neutrino searches at the LHC*, *Phys. Rev.* **D 85** (2012) 091301 [arXiv:1203.5998] [INSPIRE].

[32] S.P. Das, F.F. Deppisch, O. Kittel and J.W.F. Valle, *Heavy neutrinos and lepton flavour violation in left-right symmetric models at the LHC*, *Phys. Rev.* **D 86** (2012) 055006 [arXiv:1206.0256] [INSPIRE].

[33] J.A. Aguilar-Saavedra and F.R. Joaquim, *Measuring heavy neutrino couplings at the LHC*, *Phys. Rev.* **D 86** (2012) 073005 [arXiv:1207.4193] [INSPIRE].

[34] T. Han, I. Lewis, R. Ruiz and Z.-g. Si, *Lepton number violation and W' chiral couplings at the LHC*, *Phys. Rev.* **D 87** (2013) 035011 [arXiv:1211.6447] [INSPIRE].

[35] C.-Y. Chen, P.S.B. Dev and R.N. Mohapatra, *Probing heavy-light neutrino mixing in left-right seesaw models at the LHC*, *Phys. Rev.* **D 88** (2013) 033014 [arXiv:1306.2342] [INSPIRE].

[36] P.S.B. Dev, A. Pilaftsis and U.-k. Yang, *New production mechanism for heavy neutrinos at the LHC*, *Phys. Rev. Lett.* **112** (2014) 081801 [arXiv:1308.2209] [INSPIRE].

[37] H. Davoudiasl and I.M. Lewis, *Right-handed neutrinos as the origin of the electroweak scale*, *Phys. Rev.* **D 90** (2014) 033003 [arXiv:1404.6260] [INSPIRE].

[38] D. Binosi and L. Theussl, *JaxoDraw: a graphical user interface for drawing Feynman diagrams*, *Comput. Phys. Commun.* **161** (2004) 76 [hep-ph/0309015] [INSPIRE].

[39] CMS collaboration, *Search for heavy Majorana neutrinos in $\mu^+\mu^+[\mu^-\mu^-]$ and $e^+e^+[e^-e^-]$ events in pp collisions at $\sqrt{s} = 7$ TeV*, *Phys. Lett.* **B 717** (2012) 109 [arXiv:1207.6079] [INSPIRE].

[40] ATLAS collaboration, *Search for Majorana neutrino production in pp collisions at $\sqrt{s}$=7 TeV in dimuon final states with the ATLAS detector*, ATLAS-CONF-2012-139 (2012).

[41] LHCb collaboration, *Searches for Majorana neutrinos in B^- decays*, *Phys. Rev.* **D 85** (2012) 112004 [arXiv:1201.5600] [INSPIRE].

[42] G. Bélanger, F. Boudjema, D. London and H. Nadeau, *Inverse neutrinoless double beta decay revisited*, *Phys. Rev.* **D 53** (1996) 6292 [hep-ph/9508317] [INSPIRE].

[43] P. Benes, A. Faessler, F. Simkovic and S. Kovalenko, *Sterile neutrinos in neutrinoless double beta decay*, *Phys. Rev.* **D 71** (2005) 077901 [hep-ph/0501295] [INSPIRE].

[44] E. Nardi, E. Roulet and D. Tommasini, *Limits on neutrino mixing with new heavy particles*, *Phys. Lett.* **B 327** (1994) 319 [hep-ph/9402224] [INSPIRE].

JHEP02(2015)072

[45] E. Nardi, E. Roulet and D. Tommasini, *New neutral gauge bosons and new heavy fermions in the light of the new LEP data*, *Phys. Lett.* **B 344** (1995) 225 [hep-ph/9409310] [INSPIRE].

[46] F. del Aguila, J. de Blas and M. Pérez-Victoria, *Effects of new leptons in electroweak precision data*, *Phys. Rev.* **D 78** (2008) 013010 [arXiv:0803.4008] [INSPIRE].

[47] S. Antusch and O. Fischer, *Non-unitarity of the leptonic mixing matrix: Present bounds and future sensitivities*, *JHEP* **1410** (2014) 94 [arXiv:1407.6607] [INSPIRE].

[48] R. Hamberg, W.L. van Neerven and T. Matsuura, *A complete calculation of the order α_s^2 correction to the Drell-Yan K factor*, *Nucl. Phys.* **B 359** (1991) 343 [*Erratum ibid.* **B 644** (2002) 403-404] [INSPIRE].

[49] V.M. Budnev, I.F. Ginzburg, G.V. Meledin and V.G. Serbo, *The two photon particle production mechanism. Physical problems. Applications. Equivalent photon approximation*, *Phys. Rept.* **15** (1975) 181 [INSPIRE].

[50] B.A. Kniehl, *Elastic ep scattering and the Weizsacker-Williams approximation*, *Phys. Lett.* **B 254** (1991) 267 [INSPIRE].

[51] M.M. Block, E.M. Gregores, F. Halzen and G. Pancheri, *Photon-proton and photon-photon scattering from nucleon-nucleon forward amplitudes*, *Phys. Rev.* **D 60** (1999) 054024 [hep-ph/9809403] [INSPIRE].

[52] M. Gluck, C. Pisano and E. Reya, *The polarized and unpolarized photon content of the nucleon*, *Phys. Lett.* **B 540** (2002) 75 [hep-ph/0206126] [INSPIRE].

[53] B.E. Cox et al., *Detecting the standard model Higgs boson in the WW decay channel using forward proton tagging at the LHC*, *Eur. Phys. J.* **C 45** (2006) 401 [hep-ph/0505240] [INSPIRE].

[54] J. de Favereau de Jeneret et al., *High energy photon interactions at the LHC*, arXiv:0908.2020 [INSPIRE].

[55] D. d'Enterria and G.G. da Silveira, *Observing light-by-light scattering at the Large Hadron Collider*, *Phys. Rev. Lett.* **111** (2013) 080405 [arXiv:1305.7142] [INSPIRE].

[56] M. Drees and K. Grassie, *Parametrizations of the photon structure and applications to supersymmetric particle production at HERA*, *Z. Phys.* **C 28** (1985) 451 [INSPIRE].

[57] M. Drees, R.M. Godbole, M. Nowakowski and S.D. Rindani, *$\gamma\gamma$ processes at high-energy pp colliders*, *Phys. Rev.* **D 50** (1994) 2335 [hep-ph/9403368] [INSPIRE].

[58] V.A. Khoze, A.D. Martin and M.G. Ryskin, *Prospects for new physics observations in diffractive processes at the LHC and Tevatron*, *Eur. Phys. J.* **C 23** (2002) 311 [hep-ph/0111078] [INSPIRE].

[59] T. Han, B. Mukhopadhyaya, Z. Si and K. Wang, *Pair production of doubly-charged scalars: neutrino mass constraints and signals at the LHC*, *Phys. Rev.* **D 76** (2007) 075013 [arXiv:0706.0441] [INSPIRE].

[60] A. Das, P.S. Bhupal Dev and N. Okada, *Direct bounds on electroweak scale pseudo-Dirac neutrinos from $\sqrt{s} = 8$ TeV LHC data*, *Phys. Lett.* **B 735** (2014) 364 [arXiv:1405.0177] [INSPIRE].

[61] E. Chapon, C. Royon and O. Kepka, *Anomalous quartic $WW\gamma\gamma$, $ZZ\gamma\gamma$ and trilinear WW gamma couplings in two-photon processes at high luminosity at the LHC*, *Phys. Rev.* **D 81** (2010) 074003 [arXiv:0912.5161] [INSPIRE].

[62] I. Sahin and M. Koksal, *Search for electromagnetic properties of the neutrinos at the LHC*, *JHEP* **03** (2011) 100 [arXiv:1010.3434] [INSPIRE].

JHEP02(2015)072

[63] R.S. Gupta, *Probing quartic neutral gauge boson couplings using diffractive photon fusion at the LHC*, *Phys. Rev.* **D 85** (2012) 014006 [arXiv:1111.3354] [INSPIRE].

[64] I. Sahin, *Electromagnetic properties of the neutrinos in gamma-proton collision at the LHC*, *Phys. Rev.* **D 85** (2012) 033002 [arXiv:1201.4364] [INSPIRE].

[65] I. Sahin and B. Sahin, *Anomalous quartic $ZZ\gamma\gamma$ couplings in γp collision at the LHC*, *Phys. Rev.* **D 86** (2012) 115001 [arXiv:1211.3100] [INSPIRE].

[66] DELPHI collaboration, P. Abreu et al., *First evidence of hard scattering processes in single tagged $\gamma\gamma$ collisions*, *Phys. Lett.* **B 342** (1995) 402 [INSPIRE].

[67] CMS collaboration, *Exclusive photon-photon production of muon pairs in proton-proton collisions at $\sqrt{s} = 7$ TeV*, *JHEP* **01** (2012) 052 [arXiv:1111.5536] [INSPIRE].

[68] CMS collaboration, *Study of exclusive two-photon production of W^+W^- in pp collisions at $\sqrt{s} = 7$ TeV and constraints on anomalous quartic gauge couplings*, *JHEP* **07** (2013) 116 [arXiv:1305.5596] [INSPIRE].

[69] H1 collaboration, S. Aid et al., *Elastic and inelastic photoproduction of J/ψ mesons at HERA*, *Nucl. Phys.* **B 472** (1996) 3 [hep-ex/9603005] [INSPIRE].

[70] H1 collaboration, C. Adloff et al., *Elastic photoproduction of J/ψ and Υ mesons at HERA*, *Phys. Lett.* **B 483** (2000) 23 [hep-ex/0003020] [INSPIRE].

[71] M. Drees and D. Zeppenfeld, *Production of supersymmetric particles in elastic ep collisions*, *Phys. Rev.* **D 39** (1989) 2536 [INSPIRE].

[72] A.D. Martin, R.G. Roberts, W.J. Stirling and R.S. Thorne, *Parton distributions incorporating QED contributions*, *Eur. Phys. J.* **C 39** (2005) 155 [hep-ph/0411040] [INSPIRE].

[73] J. Pumplin et al., *New generation of parton distributions with uncertainties from global QCD analysis*, *JHEP* **07** (2002) 012 [hep-ph/0201195] [INSPIRE].

[74] C.-H. Lee, P.S. Bhupal Dev and R.N. Mohapatra, *Natural TeV-scale left-right seesaw mechanism for neutrinos and experimental tests*, *Phys. Rev.* **D 88** (2013) 093010 [arXiv:1309.0774] [INSPIRE].

[75] T. Hahn, *CUBA: a library for multidimensional numerical integration*, *Comput. Phys. Commun.* **168** (2005) 78 [hep-ph/0404043] [INSPIRE].

[76] A. Alloul, N.D. Christensen, C. Degrande, C. Duhr and B. Fuks, *FeynRules 2.0 — A complete toolbox for tree-level phenomenology*, *Comput. Phys. Commun.* **185** (2014) 2250 [arXiv:1310.1921] [INSPIRE].

[77] N.D. Christensen and C. Duhr, *FeynRules — Feynman rules made easy*, *Comput. Phys. Commun.* **180** (2009) 1614 [arXiv:0806.4194] [INSPIRE].

[78] J. Alwall et al., *The automated computation of tree-level and next-to-leading order differential cross sections and their matching to parton shower simulations*, *JHEP* **07** (2014) 079 [arXiv:1405.0301] [INSPIRE].

[79] Particle Data Group collaboration, J. Beringer et al., *Review of particle physics*, *Phys. Rev.* **D 86** (2012) 010001 [INSPIRE].

[80] R. Gavin, Y. Li, F. Petriello and S. Quackenbush, *FEWZ 2.0: a code for hadronic Z production at next-to-next-to-leading order*, *Comput. Phys. Commun.* **182** (2011) 2388 [arXiv:1011.3540] [INSPIRE].

[81] R. Gavin, Y. Li, F. Petriello and S. Quackenbush, *W physics at the LHC with FEWZ 2.1*, *Comput. Phys. Commun.* **184** (2013) 208 [arXiv:1201.5896] [INSPIRE].

JHEP02(2015)072

[82] M. Nemevšek, F. Nesti, G. Senjanović and Y. Zhang, *First limits on left-right symmetry scale from LHC data*, *Phys. Rev.* **D 83** (2011) 115014 [arXiv:1103.1627] [INSPIRE].

[83] CMS collaboration, *Search for leptonic decays of W' bosons in pp collisions at $\sqrt{s} = 7$ TeV*, *JHEP* **08** (2012) 023 [arXiv:1204.4764] [INSPIRE].

[84] A. Avetisyan et al., *Methods and results for standard model event generation at $\sqrt{s} = 14$ TeV, 33 TeV and 100 TeV proton colliders (a Snowmass whitepaper)*, arXiv:1308.1636 [INSPIRE].

[85] J. Alwall and G. Ingelman, *Interpretation of electron proton scattering at low Q^2*, *Phys. Lett.* **B 596** (2004) 77 [hep-ph/0402248] [INSPIRE].

[86] E.J. Williams, *Nature of the high-energy particles of penetrating radiation and status of ionization and radiation formulae*, *Phys. Rev.* **45** (1934) 729 [INSPIRE].

[87] C.F. von Weizsacker, *Radiation emitted in collisions of very fast electrons*, *Z. Phys.* **88** (1934) 612 [INSPIRE].

[88] ATLAS collaboration, *Expected performance of the ATLAS experiment — Detector, trigger and physics*, arXiv:0901.0512 [INSPIRE].

[89] CMS collaboration, *Identification of b-quark jets with the CMS experiment*, 2013 *JINST* **8** P04013 [arXiv:1211.4462] [INSPIRE].

[90] J.M. Campbell and R.K. Ellis, *$t\bar{t}W^{\pm}$ production and decay at NLO*, *JHEP* **07** (2012) 052 [arXiv:1204.5678] [INSPIRE].

[91] ATLAS collaboration, *Inclusive search for same-sign dilepton signatures in pp collisions at $\sqrt{s} = 7$ TeV with the ATLAS detector*, *JHEP* **10** (2011) 107 [arXiv:1108.0366] [INSPIRE].

[92] CMS collaboration, *Search for new physics with same-sign isolated dilepton events with jets and missing transverse energy at the LHC*, *JHEP* **06** (2011) 077 [arXiv:1104.3168] [INSPIRE].

[93] T. Binoth, G. Ossola, C.G. Papadopoulos and R. Pittau, *NLO QCD corrections to tri-boson production*, *JHEP* **06** (2008) 082 [arXiv:0804.0350] [INSPIRE].

[94] A. Belyaev, N.D. Christensen and A. Pukhov, *CalcHEP 3.4 for collider physics within and beyond the Standard Model*, *Comput. Phys. Commun.* **184** (2013) 1729 [arXiv:1207.6082] [INSPIRE].

[95] J.J. Sakurai and D. Schildknecht, *Generalized vector dominance and inelastic electron-proton scattering*, *Phys. Lett.* **B 40** (1972) 121 [INSPIRE].

[96] M.R. Whalley, D. Bourilkov and R.C. Group, *The Les Houches accord PDFs (LHAPDF) and LHAGLUE*, hep-ph/0508110 [INSPIRE].

[97] NNPDF collaboration, R.D. Ball et al., *Parton distributions with QED corrections*, *Nucl. Phys.* **B 877** (2013) 290 [arXiv:1308.0598] [INSPIRE].

JHEP02(2015)072